LIRGS WITH THE SMA

LUMINOUS INFRARED GALAXIES WITH THE

SUBMILLIMETER ARRAY

By

KAZIMIERZ SLIWA, B.Sc., M.Sc.

A Thesis

Submitted to the School of Graduate Studies

in Partial Fulfillment of the Requirements

for the Degree of

Doctor of Philosophy

McMaster University

DOCTOR OF PHILOSOPHY (2015)   McMaster University

(Physics and Astronomy)   Hamilton, Ontario

TITLE: Luminous Infrared Galaxies with the Submillimeter Array

AUTHOR: Kazimierz Sliwa, B.Sc. (University of Toronto), M.Sc. (McMaster University)

SUPERVISOR: Professor Christine Wilson

NUMBER OF PAGES: ??

Abstract

To my parents

Co-Authorship

Chapters 2,3,4

Acknowledgements

Table of Contents

List of Figures

List of Tables

List of Acronyms

AGN Active Galactic Nucleus

ALMA Atacama Large Millimeter/submillimeter Array

FIR Far-infrared

FWHM Full-Width at Half-Maximum

ISM Interstellar Medium

JCMT James Clerk Maxwell Telescope

LIRG Luminous Infrared Galaxy

SMA Submillimeter Array

ULIRG Ultra Luminous Infrared Galaxy

Chapter **1**

Introduction

"Astronomy compels the soul to look upwards and leads us from this world to another."

Plato (427 BC - 347 BC)

[1] What LIRGs and ULIRGs are? History, definition [2] Wavelength by wavelength findings? [3] On the individual sources? [4] Radiative Transfer [5] What we know about the molecular gas in these systems [6] The data? [7]

Chapter **2**

Luminous Infrared Galaxies with the Submillimeter Array. IV. ^{12}CO J=6-5 Observations of VV 114

"Theories crumble, but good observations never fade."

HARLOW SHAPLEY (1885 - 1972)

2.1 Introduction

Current ground-based high-resolution observations of molecular gas traced by CO for nearby galaxies are generally limited to the first three rotational transitions (J=1-0, J=2-1, and J=3-2). The *Fourier Transform Spectrometer* (FTS) aboard the *Herschel Space Observatory* has allowed us to observe higher-J transitions of nearby galaxies but at the cost of angular and spectral resolution with most ultra/luminous infrared galaxies (U/LIRGs) being point-like within the FTS beam. The higher-J transitions allow us to trace

the hot (> 100 K) molecular gas that is heated by massive young stars, X-ray dominated regions (XDRs; Maloney et al. 1996), shocks (Meijerink et al., 2013), low-energy cosmic ray protons (Goldsmith & Langer 1978) or mechanical heating (Rangwala et al. 2011) . The Submillimeter Array (SMA; Ho et al. 2004) has a receiver which provides access to the 690 GHz atmospheric window; however, observations in this window are extremely difficult due to the lack of calibrators and the poor atmospheric transmission. Thus, high angular resolution observations of higher J-level CO transitions have been extremely challenging to date. Observations with the SMA, however, provide a preview to the type of observations that will be possible with the larger collecting area of the Atacama Large Millimeter/submillimeter Array (ALMA).

Over the past two decades several starbursts have been observed in ^{12}CO J=6-5 using single dish telescopes (e.g Papadopoulos et al. 2012 and references within). Some of the first detections of ^{12}CO J=6-5 were towards the starbursts NGC 253, IC 342 and M82 (Harris et al. 1991) where it was shown that the molecular gas in starbursts is warmer than in normal disk galaxies. The only ULIRG to be observed in high-resolution ^{12}CO J=6-5 emission, to date, has been Arp 220 (Matsushita et al. 2009) using the SMA. Both nuclei of Arp 220 were detected in ^{12}CO J=6-5 and 435 μm continuum emission. Matsushita et al. (2009) find that the nuclei of Arp 220 have very similar ^{12}CO spectral line energy distributions (SLEDs) to M82 implying similar molecular gas excitation conditions and a density of $\geq 10^{3.3}$ cm^{-3} or a temperature of ≥ 30 K. However, using the CO SLED from CO $J = 1$-0 to CO $J = 13$-12, Rangwala et al. (2011) find an H$_2$ component that is significantly warmer (1350 K) than the 500 K component seen in M82 by Kamenetzky et al. (2012).

VV 114 (Arp 236, IC 1623, IRAS 01053-1746) is a nearby LIRG at a

distance of 86 Mpc (H_o = 70.5 km s^{-1} Mpc^{-1}, Ω_M = 0.27, Ω_Λ = 0.73; $1''$= 417 pc) with a far-infrared luminosity of L_{FIR}= 3.16 $\times$ 10^{11} $L_\odot$ (Sanders et al. 2003). The two merging galaxies have a projected separation of 15$''$ (6.3 kpc; Frayer et al. 1999). U et al. (2012) have derived a dust temperature of 31.45 $\pm$ 0.15 K and a dust mass of 2.6 $\times$ 10^7 $M_\odot$ by fitting a spectral energy distribution (SED) to the entire galaxy. Yun et al. (1994) observed VV 114 in ^{12}CO J=1-0 and found large amounts of molecular gas within a bar-like morphology. Le Floc'h et al. (2002) found evidence of an active galactic nucleus (AGN) associated with the eastern galaxy (VV 114E), which is the brighter of the two nuclei in the near-infrared (Scoville et al., 2000) but highly obscured in the optical (Knop et al., 1994). Iono et al. (2013) have shown that VV 114E has a high HCN/HCO$^+$ J=4-3 line ratio which further supports an AGN within VV 114E.

VV 114 is one of fourteen U/LIRGs in the SMA sample of Wilson et al. (2008; hereafter Paper I). Compared to submillimeter galaxies (SMGs), local U/LIRGs are more compact (0.3 - 3.1 kpc) than SMGs (3 - 16 kpc; Iono et al. 2009; Paper II). In an earlier paper, (Sliwa et al. 2012, Paper III), we used the radiative transfer code, RADEX (van der Tak et al., 2007) to constrain the physical conditions of the molecular gas in the three regions of Arp 299. In this paper, we present high-resolution observations of ^{12}CO J=6-5 of VV 114 using the SMA. In Section 2, we present the observations and the data reduction process of ^{12}CO J=6-5, and the recovery of the short spacings of the SMA ^{12}CO J=2-1 and ^{12}CO J=3-2 maps published in Wilson et al. (2008). In Section 3, we present line ratio maps of VV 114. In Section 4, we discuss the ^{12}CO J=6-5 emission of VV 114. In Section 5, we present our radiative transfer modeling results. In Section 6, we discuss the implications of the

low ^{13}CO abundance and use our modeling results to constrain the CO-to-H$_2$ conversion factor in VV 114.

2.2 Observations and Data Reduction

2.2.1 ^{12}CO J=6-5 Submillimeter Array Data

The ^{12}CO J=6-5 emission in VV 114 was observed with the SMA on 2008 August 26 using a two-point mosaic. Although eight antennas were available, we used only the six antennas that were placed in the innermost ring of the subcompact configuration to reduce resolution effects (i.e. avoid resolving out flux). This resulted in baselines ranging between 10 m and 25 m which corresponds to an angular resolution of $3.1''\times2.2''$. The upper sideband (USB) of the 690 GHz receiver was tuned to the redshifted ^{12}CO J=6-5 line at 677.870 GHz leaving the lower sideband (LSB), separated by 10 GHz, for continuum measurements. Each sideband had a width of 2 GHz with a spectral resolution of 0.8125 MHz. Weather conditions were excellent throughout the track with an opacity at 225 GHz around 0.02 - 0.06 corresponding to a precipitable water vapour of $\sim$0.5 - 1.0 mm. This corresponds to system temperatures below 600 K.

Data reduction was done with the IDL MIR package. The bandpass was calibrated on Uranus, Callisto and 3C454.3. The time variable gain calibration was performed on Uranus which was within 20 degrees of VV 114 at the time of the observations. Uranus had a diameter of 3.6" on the observation date and thus was slightly resolved. We used a standard planet visibility model (a uniform disk) in analyzing the Uranus uv-data. The absolute flux scale was set using Uranus and checked using Callisto suggesting an accuracy level of

the flux calibration of 20%. The calibrated uv-data were converted to FITS format and then imported into CASA for further processing and imaging. The uv-data were flagged to remove outlier data points with high amplitude values and the continuum was subtracted using line-free channels. We created a clean data cube with velocity resolution of 20 km s^{-1} using a robust weighting scheme. The dataset was cleaned down to two times the rms noise level of 270 mJy beam^{-1} in each 20 km s^{-1} velocity channel. An integrated intensity map was created using channels with emission greater than the 2σ cutoff. The integrated intensity map has been corrected for the primary beam (Figure 1). The peak spectrum of VV 114E is shown in Figure 2.

2.2.2   Additional CO Data

VV 114 was observed at the SMA in ^{12}CO J=3-2 on 2006 November 12 and ^{12}CO J=2-1 on 2006 November 24. The observations and calibration details are given in Paper I. The ^{13}CO J=2-1 line was observed in the LSB simultaneously with ^{12}CO J=2-1. The calibrated uv-data from Paper I, in FITS format, were imported into CASA for further processing and imaging. The datasets were processed similarly to the ^{12}CO J=6-5 data set (see above and Figures 15 and 16 of Paper I).

We have obtained a natural weighted clean cube of ^{12}CO J=1-0 observed with the Owens Valley Radio Observatory (OVRO) first published in Yun et al. (1994). Details of the observations and reduction are given in Yun et al. (1994). We created an integrated intensity map with a 2σ cutoff using velocity channels with emission from VV 114. VV 114 was observed with ALMA during cycle 0 in ^{13}CO J=1-0 (Saito et al. in prep.) using the compact

configuration. We obtained calibrated uv-data from the ALMA archive. The uv-data were continuum subtracted using line-free channels and a 40 km s^{-1} cleaned datacube was created. We created an integrated intensity map with a 2σ cutoff using velocity channels with emission from VV 114 (see Figure 1).

All integrated intensity maps were corrected for the primary beam. Table 1 presents the observational information for VV 114.

The James Clerk Maxwell Telescope (JCMT) was used to map VV 114 in ^{12}CO J=3-2 using the RxB3 receiver on 2005 August 17 (Program: M05AC05; PI: C.D. Wilson) and ^{12}CO J=2-1 using the RxA3 receiver on 2012 November 26 (Program: M12BC14; PI: K. Sliwa). The ^{12}CO J=3-2 map covered 35″ on each side with a 14″ beam and the ^{12}CO J=2-1 map covered 49″ on side with a 21″ beam which included all the emission from VV 114. For the ^{12}CO J=3-2 reduction refer to Paper I. The raw ^{12}CO J=2-1 data were made into a cube spanning -600 km s^{-1} to 600 km s^{-1} using the `Starlink` software (Currie et al. 2008). Using line-free channels, the cube was continuum corrected using a first-order baseline. The velocity resolution of the cube was binned to 20 km s^{-1}. We assume a main beam efficiency (η_{mb}) of 0.6 for ^{12}CO J=3-2 and 0.69 for ^{12}CO J=2-1 in order to convert the intrinsic units of antenna temperature (T_A^*) to main beam temperature ($T_{mb} = T_A^*/\eta_{mb}$) and then to Jy km s^{-1} which gives us a scaling factor of 26.9 Jy K $(T_{mb})^{-1}$ and 22.9 Jy K $(T_{mb})^{-1}$ for ^{12}CO J=3-2 and ^{12}CO J=2-1 respectively. Similarly to Sliwa et al. (2012) with Arp 299, we assume that emission from VV 114 fills the beam, unlike Paper I where VV 114 was treated like a point source.

When we compare the SMA-only map to the JCMT map, the ^{12}CO J=3-2 map is missing about 60% and the ^{12}CO J=2-1 map about 46% of the total flux (see Table 1). Note that Paper I estimated only 48% for ^{12}CO J=3-2

because they assumed VV 114 to be point-like in the K to Jy conversion of the JCMT map.

We recover the short spacings of the ^{12}CO J=2-1 and ^{12}CO J=3-2 SMA datasets using the JCMT datasets. The recovery of short spacings using single dish data is still a process under development and it will become a common practice in the ALMA era. The two datasets were combined in the image plane using the "feathering" technique (Stanimirovic 2002). We use the the method of Paper III assuming the flux scales of both datasets to be the same. Figure 1 presents the integrated intensity maps of ^{12}CO J=2-1 and ^{12}CO J=3-2 with short spacings recovered. For comparison, see Figures 15 and 16 of Paper I for the SMA-only integrated intensity maps. Both short spacings recovered maps show significant increases in flux (see Figure 1 and Table 1). Negative flux (dashed contours in Figure 1), usually a sign of the missing flux problem, is still seen in the ^{12}CO J=3-2 map; however, negative flux can also be caused by the uv-coverage of the map (Stanimirovic 1999). Since the negative flux caused by the uv-coverage cannot be quantified, adjusting the flux scales of the datasets may introduce artificial emission into our maps. We, therefore, attribute the negative flux seen to the poor uv-coverage of the SMA maps that transfer into the short spacings recovered maps.

2.3   Line Ratio Maps

We have degraded the resolution of all the maps to the resolution of the OVRO ^{12}CO J=1-0 map, $6.5'' \times 3.7''$. This ensures that we are probing the molecular gas of VV 114 on similar physical scales ($\sim$ 2 kpc). We applied a Gaussian taper to the observations to degrade the resolution. We created new integrated

intensity maps and corrected for the primary beam. The intrinsic units of the CO integrated maps were converted from Jy beam^{-1} km s^{-1} to K km s^{-1}. Line ratio maps of ^{12}CO (J=6-5)/(J=3-2), ^{12}CO (J=3-2)/(J=2-1), ^{12}CO (J=2-1)/(J=1-0), ^{13}CO (J=2-1)/(J=1-0), (^{12}CO/^{13}CO) J=1-0 and (^{12}CO/^{13}CO) J=2-1 were created by dividing the appropriate maps with a 2σ cutoff for each map (Figures 3 and 4). Emission near the edges of the maps was masked out. Note that the line ratio values at the edges of VV 114 are noisier because the uncertainty approaches $\pm 50\%$. Table 2 presents the line ratios at the peak position of ^{12}CO J=3-2 emission in each of the three regions.

In Paper III, it was found that at the peak position for each nucleus and the overlap region of Arp 299, the missing flux was insignificant ($<<1\%$) in both the ^{12}CO J=2-1 and ^{12}CO J=3-2 maps. This is not the case for VV 114 and indicates that the short spacings are important in this galaxy. However, when we compare the intensity of the short spacings corrected maps to the SMA-only maps near the peak position of VV 114E, we see that only 10-15% of flux is missing in the ^{12}CO J=3-2 and ^{12}CO J=2-1 maps, well within our calibration uncertainty. Thus, the line ratios at VV 114E are roughly similar whether or not the short spacing data are included (see Figure 3 and Table 2), and we assume the same for the other ratio maps around the peak position of VV 114E.

2.4 ^{12}CO J=6-5 Emission

The ^{12}CO J=6-5 line is only detected in VV 114E (Figure 1 and 2). The other two sources $>3\sigma$ in the map do not have any counterpart in the ^{12}CO J=3-2 map or spectrum, and are thus likely to be artifacts. The total flux

of ^{12}CO J=6-5 in the SMA map is 150 ± 40 Jy km s^{-1}. Since there are no ^{12}CO J=6-5 single dish maps of VV 114, we use an archival *Herschel* FTS spectrum to estimate the missing flux. The total flux of the ^{12}CO J=6-5 line is 1390 ± 100 Jy km s^{-1} from the FTS spectrum (M.R.P. Schirm 2013, private communication) and when compared to the SMA map, we are missing 89 ± 10 % of the flux. The missing flux indicates that short spacings are increasingly important at higher observing frequencies for VV 114.

If we assume the same ^{12}CO(J=6-5)/(J=3-2) line ratio for the central (VV 114C) and western (VV 114W) regions as for VV 114E, we can estimate the expected peak intensity of ^{12}CO J=6-5 of the other two regions. This estimate yields 130 and 70 Jy beam^{-1} km s^{-1} for VV 114C and VV 114W regions respectively and suggests that we should have detected the other two regions at $\geq 4\sigma$ level. This situation could be explained by two scenarios: the emitting ^{12}CO J=6-5 sources in these two regions are on larger scales that are filtered out with the SMA or the ^{12}CO(J=6-5)/(J=3-2) line ratio is quite different from VV 114E indicating different physical conditions. If we assume the former to be true, the *Herschel* FTS observations cannot be used to recover the missing flux in the SMA map; a single dish ^{12}CO J=6-5 map is required to recover the flux. If we assume the latter to be true, we can use the 3σ level of the ^{12}CO J=6-5 map and the peak intensity in the ^{12}CO J=3-2 SMA map to put an upper limit to the ^{12}CO(J=6-5)/(J=3-2) line ratio (see Table 2).

We compare the ^{12}CO J=6-5 maps of VV 114 and Arp 220 (Matsushita et al. 2009). The SMA ^{12}CO J=6-5 observations of Arp 220 kinematically resolved the two nuclei. When comparing the SMA ^{12}CO J=6-5 flux of Arp 220 with the *Herschel FTS* flux (Rangwala et al. 2011), the SMA map is

missing 69 ± 7 %. More ^{12}CO J=6-5 emission is recovered in Arp 220 with the SMA which suggests that the ^{12}CO J=6-5 emission is more compact than in VV 114. The ^{12}CO (J=6-5)/(J=3-2) line ratios of the two nuclei of Arp 220 are nearly five times higher than for VV 114E indicating that the molecular gas is more excited in Arp 220 than in VV 114. Rangwala et al. (2011) have found evidence of a very hot ($T_{\mathrm{kin}} = 1350$ K) molecular gas component which may explain the higher observed ^{12}CO (J=6-5)/(J=3-2) line ratio. The ^{12}CO (J=6-5)/(J=3-2) line ratio for M82 (~ 0.35; Kamenetzky et al. 2012) is also higher than that of VV 114E. The hot molecular gas component of M82 (T_{kin} = 500 K; Kamenetzky et al. 2012) is cooler than of Arp 220. If the differences in the ^{12}CO (J=6-5)/(J=3-2) line ratios are due to temperature differences, then the hot molecular gas component of VV 114E would be less than 500 K.

2.5 Molecular Gas Physical Conditions

2.5.1 Radiative Transfer Model

In order to constrain the beam-averaged physical conditions of VV 114, we use the radiative transfer code RADEX (van der Tak et al. 2007). RADEX calculates line fluxes and optical depth for specific temperature (T_{kin}), density ($n_{\mathrm{H_2}}$) and column density (N_{mol}) of the molecular species of interest.

We use RADEX to generate ^{12}CO line fluxes for a 3D grid in T_{kin} ($10^{0.7}$ - $10^{3.8}$ K), $n_{\mathrm{H_2}}$ ($10^{1.0}$ - $10^{7.0}$ cm^{-3}), and $N_{^{12}\mathrm{CO}}$ (10^{12} - 10^{18} cm^{-2}) for $dv = 1$ km s^{-1}. We use the line widths measured using the ^{12}CO J=3-2 map (see Table 3) to correct the column density for the particular region of interest in VV 114. The observed Galactic ^{13}CO abundance relative to ^{12}CO is $[^{12}$CO$]/[^{13}$CO$] = 30 - 70$ (Langer & Penzias 1990). We generate another grid for ^{13}CO using the

same parameter space as for ^{12}CO that covers the observed Galactic abundance value range ($[^{12}$CO$]/[^{13}$CO$]$ =10 – 100; Grid 1). We also generate a second ^{13}CO grid expanding the relative abundance to ^{12}CO ($[^{12}$CO$]/[^{13}$CO$]$ = 10 – 10^5; Grid 2).

2.5.2   Likelihood Analysis

In addition to RADEX, we use a Bayesian likelihood code (Ward et al. 2003, Panuzzo et al. 2010, Kamenetzky et al. 2011). The Bayesian likelihood code determines the most probable solutions for the physical conditions of the molecular gas by comparing the RADEX calculated and the observed ^{12}CO and ^{13}CO line fluxes. The likelihood code generates probability distributions for four parameters, T_{kin}, $n_{\mathrm{H_2}}$, $N_{^{12}\mathrm{CO}}$ and area filling factor (Φ_{A}). We mention some of the basic aspects of the code here but for more details on the likelihood code see Kamenetzky et al. (2012) and Rangwala et al. (2011).

The likelihood code generates two calculated values for each parameter: the 1DMax and the 4DMax. The 1DMax refers to the maximum likelihood of the given parameter based on the one-dimensional likelihood distribution for the parameter. The 4DMax is the maximum likelihood of a single grid point based on the four-dimensional likelihood distribution of the four parameters mentioned above.

We implement three priors in order to constrain the solutions to those of realistic physical conditions (Ward et al. 2003; Rangwala et al. 2011). The first prior constrains the column density to ensure that the total mass within the column does not exceed that of the dynamical mass of the system (see Rangwala et al. 2011 for more details). The dynamical mass of each region

was measured using

$$M_{\mathrm{dyn}} = 99\Delta V^2 D(\mathrm{pc}) \tag{2.1}$$

where ΔV is the line width of the system in km s^{-1} and $D(\mathrm{pc})$ is the diameter of the system in parsecs (Wilson et al. 1997; see Table 3). The ^{12}CO J=3-2 map has the best resolution and signal-to-noise ratio (SNR); therefore, we use the ^{12}CO J=3-2 map to fit each region of VV 114 to a two-dimensional Gaussian to measure the diameter (see Table 3), assuming a spherical geometry. We also use the ^{12}CO J=3-2 spectrum of each region to fit ΔV using a Gaussian profile (see Table 3).

The second prior constrains the column length to be less than the length of the molecular region. We estimate the length of the molecular region using the deconvolved source sizes (see Table 3) and assuming a spherical geometry. This prior will constrain $n_{\mathrm{H_2}}$ at the lower end and $N_{^{12}\mathrm{CO}}$ at the higher end (Rangwala et al. 2011).

The third prior constrains the optical depth to be $0 < \tau < 100$. A negative τ indicates a maser; however, we do not expect the CO lines to exhibit maser properties and, therefore, we constrain τ to be greater than zero. The upper limit of $\tau = 100$ is put in place as recommended by the RADEX documentation.

2.5.3   Modeling Results

We model the molecular gas at the peak position of ^{12}CO J=3-2 ($\alpha_{J2000} = 01^h07^m47.453^s$, $\delta_{J2000} = $ -17^{d}30^{m}25.037^s) in VV 114E. We do not have detections of ^{12}CO J=6-5 and ^{13}CO in VV 114W; therefore, we cannot model the molecular gas of VV 114W using the likelihood code (i.e. four fitted parame-

ters using three observed line fluxes).

We present two possible solutions for VV 114E, one for each of the ^{13}CO grids. The most probable solution for Grid 1 gives a hot ($T_{\text{kin}} = 390$ K), diffuse ($n_{\text{H}_2} = 10^{2.29}$ cm^{-3}) molecular gas component. The most probable [^{12}CO]/[^{13}CO] value hit the upper limit of our grid ([^{12}CO]/[^{13}CO] = 100). To see if hitting the upper limit of [^{12}CO]/[^{13}CO] affects our results, we use Grid 2 with the expanded range of values. Grid 2 shows a maximum probable solution of a cold ($T_{\text{kin}} = 38$ K), moderately dense ($n_{\text{H}_2} = 10^{2.89}$ cm^{-3}) molecular gas component (see Table 4). The most probable [^{12}CO]/[^{13}CO] value increased from 100 to 229. The difference in the solutions arises from the difference in the most probable [^{12}CO]/[^{13}CO] value showing the importance of the abundance ratio in constraining the physical conditions of the molecular gas. Figure 5 shows the ^{12}CO and ^{13}CO SLEDs with the most probable solution fit to both species. Figure 6 shows the one-dimensional probability distributions for T_{kin} n_{H_2} and $N_{^{12}\text{CO}}$ for both grid runs to show the difference in the solutions. Figure 7 shows the two-dimensional distribution for T_{kin} against n_{H_2} for Grid 2. The optical depth (τ) for the ^{12}CO lines is >>1 where $\tau \sim 14$ for ^{12}CO J=1-0 and peaks at the ^{12}CO J=4-3 line with $\tau \sim 65$ indicating that the ^{12}CO lines are optically thick. The τ for ^{13}CO peaks at the ^{13}CO J=2-1 line with $\tau \sim 1.1$ and the ^{13}CO J=1-0 $\tau \sim 0.4$.

2.6 Discussion

2.6.1 Line Ratios

Aalto et al. (1995) show that ^{13}CO (J=2-1)/(J=1-0) > ^{12}CO (J=2-1)/(J=1-0) > 1 for the majority of their sample of infrared-bright galaxies. VV 114E

shows the opposite with ^{12}CO $(J=2\text{-}1)/(J=1\text{-}0) > {}^{13}$CO $(J=2\text{-}1)/(J=1\text{-}0)$ at the ^{12}CO $J=3\text{-}2$ peak position (see Table 2). From the RADEX models, we find the excitation temperatures (T_{ex}) for ^{13}CO $J=1\text{-}0$ and ^{13}CO $J=2\text{-}1$ are ~ 14 K and ~ 8 K, respectively. Assuming similar T_{ex} as found with the RADEX models with $\tau \ll 1$ and using the equations in Section 4.2 of the RADEX manual[1], we would expect to see ^{13}CO $(J=2\text{-}1)/(J=1\text{-}0) \sim 1.4$. If both ^{13}CO $J=1\text{-}0$ and ^{13}CO $J=2\text{-}1$ lines had the same T_{ex} and the moderate optical depths as found with the likelihood analysis, we would expect a line ratio > 1.5. This analysis suggests that both moderate optical depths and subthermal excitation are required to produce ^{13}CO $(J=2\text{-}1)/(J=1\text{-}0) < 1$ in VV 114E.

2.6.2   Radiative Transfer Modeling Results

The first three ^{12}CO transition line intensities are slightly over estimated by the best fit model (see Figure 5; for ^{12}CO $J=6\text{-}5$ see below) but the best fit intensities are well within our uncertainties. In order to significantly excite ^{12}CO $J=3\text{-}2$, the molecular gas must be $T_{\text{kin}} > 30$ K. Once n_{H_2}, T_{kin} and $N_{^{12}\text{CO}}$ are large enough to thermalize ^{12}CO up to $J=3\text{-}2$, the ^{13}CO lines provide further constraints on the best fit. The ^{13}CO $(J=2\text{-}1)/(J=1\text{-}0)$ line ratio will depend on $N_{^{13}\text{CO}}$ and T_{ex} (see Section 6.1). A large $N_{^{13}\text{CO}}$ is needed to obtain the moderate optical depths required for the low observed line ratio (< 1). The best fit is likely mainly driven by the ^{13}CO lines which may explain the slight over-estimate of the ^{12}CO lines up to $J=3\text{-}2$.

The most probable solution for VV 114E is a cold $(T_{\text{kin}} = 38$ K), moderately dense $(n_{\text{H}_2} = 10^{2.89}$ cm$^{-3})$ molecular gas component. This solution is

---

[1]www.strw.leidenuniv.nl/~moldata/radex_manual.pdf

similar to what is seen in radiative transfer modeling of Arp 220 (Rangwala et al. 2011), Arp 299 (Paper III) and M82 (Kamenetzky et al. 2012) where a cold, moderately dense molecular gas component is seen. The temperature of the cold molecular gas component in M82 is much warmer ($T_{\text{kin}} = 63$ K) and the gas density is slightly higher ($n_{\text{H}_2} = 10^{3.40}$ cm^{-3}) than what we see for VV 114E. The solution for the physical conditions of VV 114E is more similar to that of the cold molecular gas component in Arp 220 ($T_{\text{kin}} = 50$K, $n_{\text{H}_2} = 10^{2.8}$ cm^{-3}). The temperature of the cold molecular gas component in Arp 220 is slightly higher than seen in VV 114E but that may be due to the difference in merger stages of the two galaxies (i.e. Arp 220 is at a more advanced merger stage than VV 114). VV 114 is believed to be a late-stage merger on the verge of experiencing more massive bursts of star formation and becoming a ULIRG (Iono et al. 2004) like Arp 220. The future starburst that VV 114 will experience may heat the cold molecular gas to the same temperature of the cold molecular gas component in Arp 220.

The *FTS* analyses of Arp 220 and M82 also shows a hot molecular gas component from excess emission above the ^{12}CO $J = 4$-3 transition. From the CO SLED of VV 114E, we do not see any excess emission at the ^{12}CO $J=6$-5 transition; indeed, the 4DMax solution overestimates the ^{12}CO $J=6$-5 flux. The overestimation of the ^{12}CO $J=6$-5 flux may be due to more missing flux than we originally assumed; however, we need a high-resolution image with short spacings to confirm this case. To constrain the hot molecular gas of VV 114 is beyond the scope of this paper, where we require other higher-J level CO transitions at high angular resolution which ALMA will eventually be able to observe.

2.6.3 ^{13}CO to ^{12}CO Abundance: [^{12}CO]/[^{13}CO]

The most probable value of [^{12}CO]/[^{13}CO] in VV 114E is roughly three times larger than the value seen in the local interstellar medium (ISM; [^{12}CO]/[^{13}CO] = 77; Wilson & Rood 1994). Casoli et al. (1992) have suggested that the observed higher ^{12}CO/^{13}CO line ratios seen in U/LIRGs than in our Galaxy are likely due to an under-abundance of ^{13}CO and/or an over-abundance of ^{12}CO. Casoli et al. (1992) also suggest several mechanisms to account for the increased [^{12}CO]/[^{13}CO] value in U/LIRGs with two mechanisms as the most likely scenarios. The starburst episodes of U/LIRGs produce numerous massive stars that can enrich the ISM in ^{12}CO via ^{12}C nucleosynthesis that can enhance the [^{12}CO]/[^{13}CO] value. Another possible mechanism to enhance [^{12}CO]/[^{13}CO] is via infalling gas with a high [^{12}CO]/[^{13}CO] value from the outer regions during the merger process. Both mechanisms can explain our results and it may be a combination of the two.

Martín et al. (2010) have placed limits on the ^{12}C/^{13}C isotopic ratio in M82 and NGC 253 to be > 138 and > 81, respectively. If we assume that the ^{12}C/^{13}C isotopic ratio reflects [^{12}CO]/[^{13}CO] then both these starbursts have larger [^{12}CO]/[^{13}CO] value than seen the local ISM. Henkel et al. (2010) have observed ^{13}CO J=3-2 in the Cloverleaf quasar and have compared it to the ^{12}CO J=3-2. The observed ^{12}CO/^{13}CO line ratio was 40 and exceeds that seen in Arp 220 but is similar to that of NGC 6240 (Greve et al. 2009). Henkel et al. (2010) surmise that the high line ratio may be caused by a real deficiency in ^{13}CO where Large Velocity Gradient (LVG) models yield [^{12}CO]/[^{13}CO] values $>> 100$. It may be quite common to find larger [^{12}CO]/[^{13}CO] values in starbursts than the value seen in the Galaxy.

2.6.4   CO-to-H_2 Conversion Factor: α_{CO}

Using the 4DMax solution for the beam-averaged column density ($<N_{^{12}CO}>$) and assuming a ^{12}CO to H_2 abundance ratio of $x_{CO} = 3$ x 10^{-4} (Ward et al. 2003), we can measure the CO-to-H_2 conversion factor (α_{CO}). We use the short spacing corrected ^{12}CO J=2-1 map to measure the peak luminosity of VV 114E because the map has recovered the flux on all scales. We convert the ^{12}CO J=2-1 luminosity to a ^{12}CO J=1-0 luminosity using the line ratio in Table 2. The total mass within the beam is $6.2^{+7.3}_{-3.7} \times 10^8$ $M_\odot$ and the luminosity of ^{12}CO J=1-0 within the beam is 1.3×10^9 K km s^{-1} pc^2. We measure α_{CO} to be $0.5^{+0.6}_{-0.3}$ $M_\odot$ (K km s^{-1} pc^2)$^{-1}$. This value agree within uncertainties with the value widely used for ULIRGs determined by Downes & Solomon (1998; $\alpha_{CO} = 0.8$ $M_\odot$ (K km s^{-1} pc^2)$^{-1}$). To recover the Downes & Solomon (1998) value, the x_{CO} value would need to be 1.6 times smaller (x_{CO} = 1.8×10^{-4}). This value for α_{CO} for VV 114E is consistent with the recent findings of Papadopoulos et al. (2012) for LIRGs using single dish observations ($\alpha_{CO} = 0.6 \pm 0.2$ $M_\odot$ (K km s^{-1} pc^2)$^{-1}$).

We can place another limit to α_{CO} using the dynamical mass (see Table 2) and the total CO luminosity of VV 114E. Because of its better angular resolution, we use the short spacings corrected ^{12}CO J=3-2 map to measure the CO luminosity of VV 114E. We assume a line ratio of 0.92 for $^{12}CO(J$=3-2)/(J=1-0) to convert the total ^{12}CO J=3-2 luminosity to total ^{12}CO J=1-0 luminosity of VV 114E ($L_{CO(1-0)} = 1.6 \times 10^9$ K km s^{-1} pc^2). Comparing this luminosity to the dynamical mass, we measure α_{CO} to be 1.5 $M_\odot$ (K km s^{-1} pc^2)$^{-1}$. Since the dynamical mass includes the mass of stars and dark matter as well as gas, and the gas in the center of VV 114E might not be in gravitational

equilibrium, the dynamical mass measured α_{CO} is strictly an upper limit. The upper limit is consistent with the radiative transfer model-derived value for α_{CO}.

Paper III measured α_{CO} of Arp 299 to be 0.4 ± 0.3 $M_{\odot}$ (K km s^{-1} pc^2)$^{-1}$. The value for Arp 299 is consistent with the value of Downes & Solomon (1998). Arp 299 is believed to be an earlier stage merger than VV 114. Schirm et al. (in prep.) have measured a value for α_{CO} in NGC 4038/39 ($\alpha_{CO} = 7$ $M_{\odot}$ (K km s^{-1} pc^2)$^{-1}$) similar to the Galactic value. NGC 4038/39 is a young merger that has not yet progressed into the LIRG stage and shows no strong evidence of an enhanced conversion factor. The α_{CO} factor may evolve as the merger process goes on instead of the currently adopted bimodal factor (i.e. Galactic or ULIRG); however, a larger sample of measured α_{CO} for U/LIRGs at different stages is needed to deduce whether an α_{CO} factor as a function of merger stage is plausible.

2.7   Conclusions

In this paper, we have presented high-resolution SMA observations of ^{12}CO J=6-5 of the nearby LIRG VV 114. We combine the new ^{12}CO J=6-5 map with the ^{12}CO J=2-1, ^{12}CO J=3-2 and ^{13}CO J=2-1 SMA maps of Wilson et al. (2008), ^{12}CO J=1-0 OVRO map of Yun et al. (1994) and ^{13}CO J=1-0 ALMA cycle 0 map of Saito et al. (in prep.) to constrain the beam-averaged physical conditions of the molecular gas.

1. We detect ^{12}CO J=6-5 emission in VV 114E. If we assume a similar ^{12}CO $(J$=6-5$)/(J$=3-2$)$ line ratio for both VV 114C and VV 114W and using the peak position flux of ^{12}CO J=3-2 we should have detected

VV 114C and VV 114W in ^{12}CO J=6-5 at >4σ level. Since we do not detect VV 114C and VV 114W, we conclude that either the physical conditions of these two regions are different from VV 114E or the ^{12}CO J=6-5 emission is extended and filtered out by the SMA.

2. We combine JCMT ^{12}CO J=2-1 and ^{12}CO J=3-2 maps with the SMA maps to recover the short spacings. We find that the missing flux around the position of the peak flux of VV 114E in both maps is $\sim 10-15\%$, well within our calibration uncertainties (20%). The missing flux in VV 114C and VV 114W is more significant, revealing the importance of short spacings for these two regions.

3. We use the radiative transfer code RADEX and a Bayesian likelihood code to constrain the physical conditions of VV 114E. We find evidence of a cold ($T_{\mathrm{kin}} = 38$ K), moderately dense ($n_{\mathrm{H_2}} = 10^{2.89}$ cm^{-3}) molecular gas component. The most probable [^{12}CO]/[^{13}CO] for VV 114 was found to be 229. We show that a lower value of [^{12}CO]/[^{13}CO] would support a hot ($T_{\mathrm{kin}} > 200$ K), diffuse ($n_{\mathrm{H_2}} < 10^{2.5}$ cm^{-3}) molecular gas component.

4. The most probable [^{12}CO]/[^{13}CO] is roughly three times larger than seen for the local ISM and may explain the high ^{12}CO/^{13}CO line ratios (> 25) observed for VV 114E.

5. We use the most probable $<N_{^{12}\mathrm{CO}}>$ and the peak position luminosity of ^{12}CO J=1-0 to measure the CO-to-H$_2$ conversion factor, α_{CO}. We measure α_{CO} to be $0.5^{+0.6}_{-0.3}$ $M_\odot$ (K km s^{-1} pc^2)$^{-1}$ for VV 114E, which agrees with the widely used factor of Downes & Solomon (1998). Using the dynamical mass and the total CO luminosity of VV 114E, we place

an upper limit to α_{CO} to be $\leq 1.5\ M_\odot\ (\text{K km s}^{-1}\ \text{pc}^2)^{-1}$.

ALMA will eventually make observations of VV 114 in ^{12}CO J=6-5 that will include the short spacings from the Atacama Compact Array (ACA). Combining the ALMA ^{12}CO J=6-5 observations with the new short spacings recovered SMA ^{12}CO J=2-1 and ^{12}CO J=3-2 maps will allow us to constrain the physical conditions of the molecular gas over the full extent of the galaxy using a similar approach to this paper. There is also evidence that a hot molecular gas component exists in starburst galaxies (Rangwala et al. 2011, Kamenetzky et al. 2012); however, to constrain the physical conditions of the hot molecular gas component, higher-J CO transitions are required. ALMA will one day be able to observe VV 114 in ^{12}CO J=4-3 (band 8), J=7-6 and J=8-7 (band 10) at high angular resolutions that will be used to constrain the physical conditions of the hot molecular gas component.
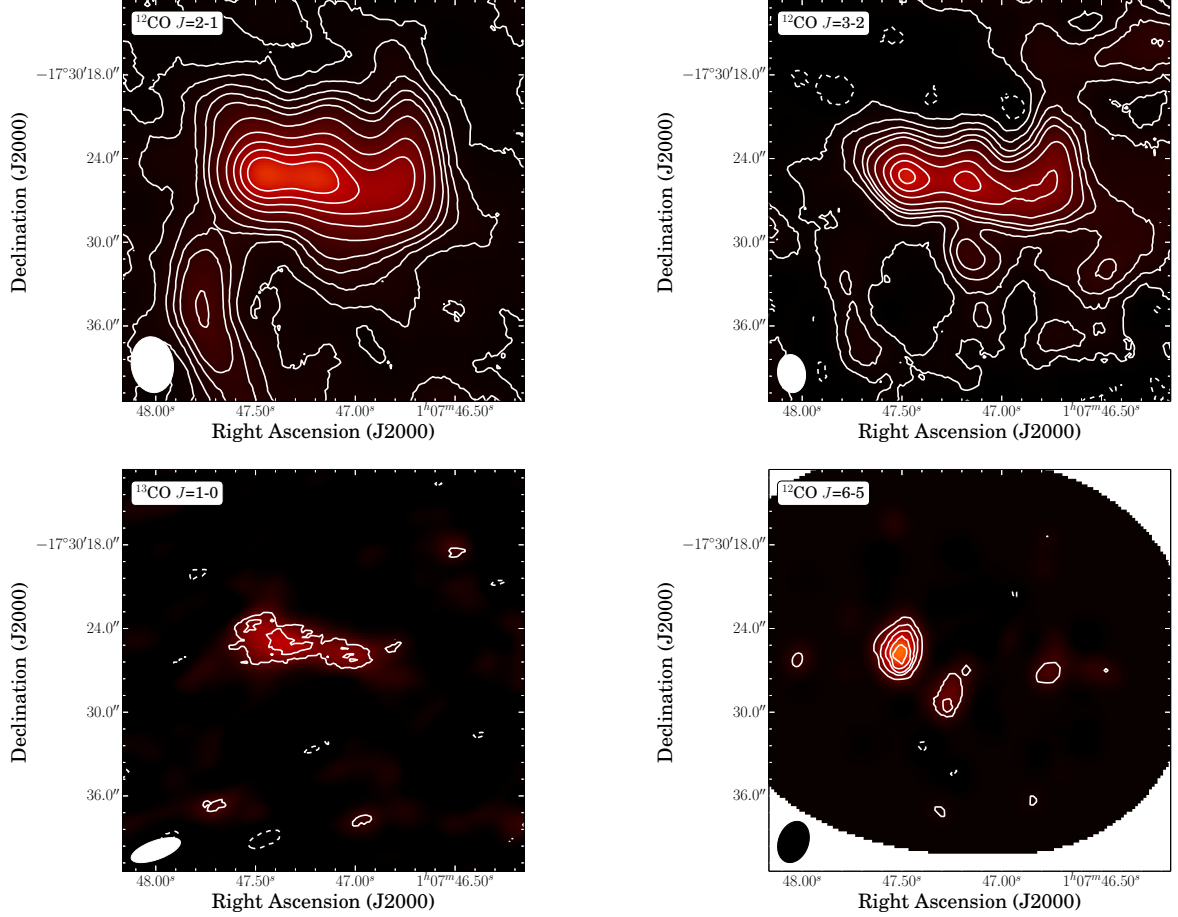
=

Figure 2.1 (*Top Left*) ^{12}CO J=2-1 map with the recovered short spacings from the JCMT. The contours correspond to -7.5, -4.5, -1.5, 1.5, 4.5, 7.5, 10.5, 13.5, 20, 30, 40, 50, 60 $\times$ 3.5 Jy beam^{-1} km s^{-1} (*Top Right*) ^{12}CO J=3-2 map with the recovered short spacings from the JCMT. The contours correspond to -7.5, -4.5, -1.5, 1.5, 4.5, 7.5, 10.5, 13.5, 20, 30, 40, 50 $\times$ 7 Jy beam^{-1} km s^{-1}. (*Bottom Left*) ^{13}CO *J*=1-0 map with contours corresponding to -2, 2, 4, 6 $\times$ the 1σ value of 0.25 Jy beam^{-1} km s^{-1}. (*Bottom Right*) ^{12}CO *J*=6-5 map with contours corresponding to –2, 2, 4, 6, 8, 10 $\times$ the 1σ value of 16.4 Jy beam^{-1} km s^{-1}. All maps have been corrected for the primary beam. Negative flux is denoted by dashed contours.
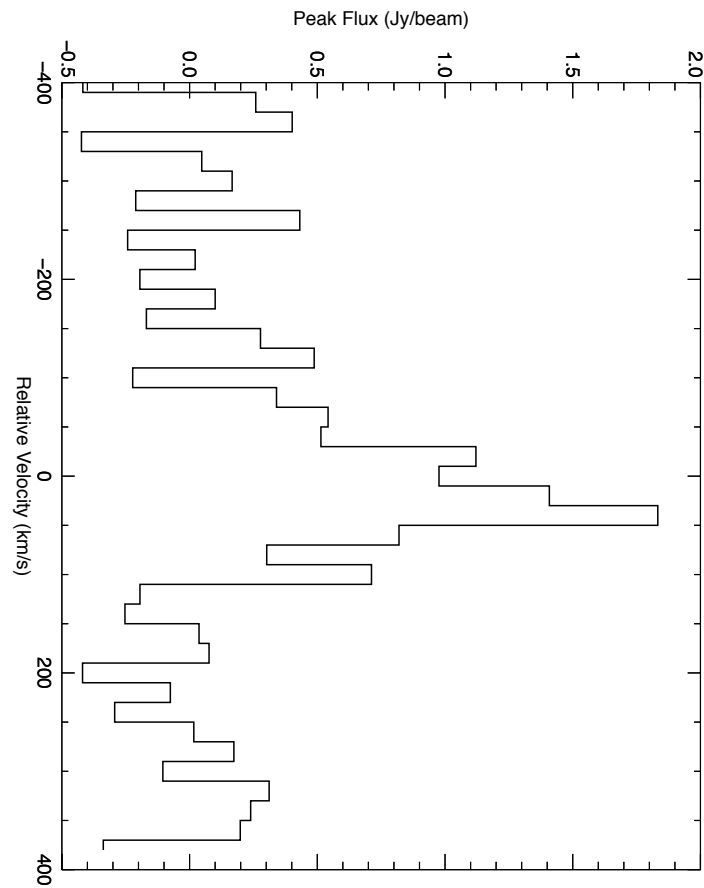
Figure 2.2 Peak spectrum of the ^{12}CO J=6-5 emission for VV 114E.
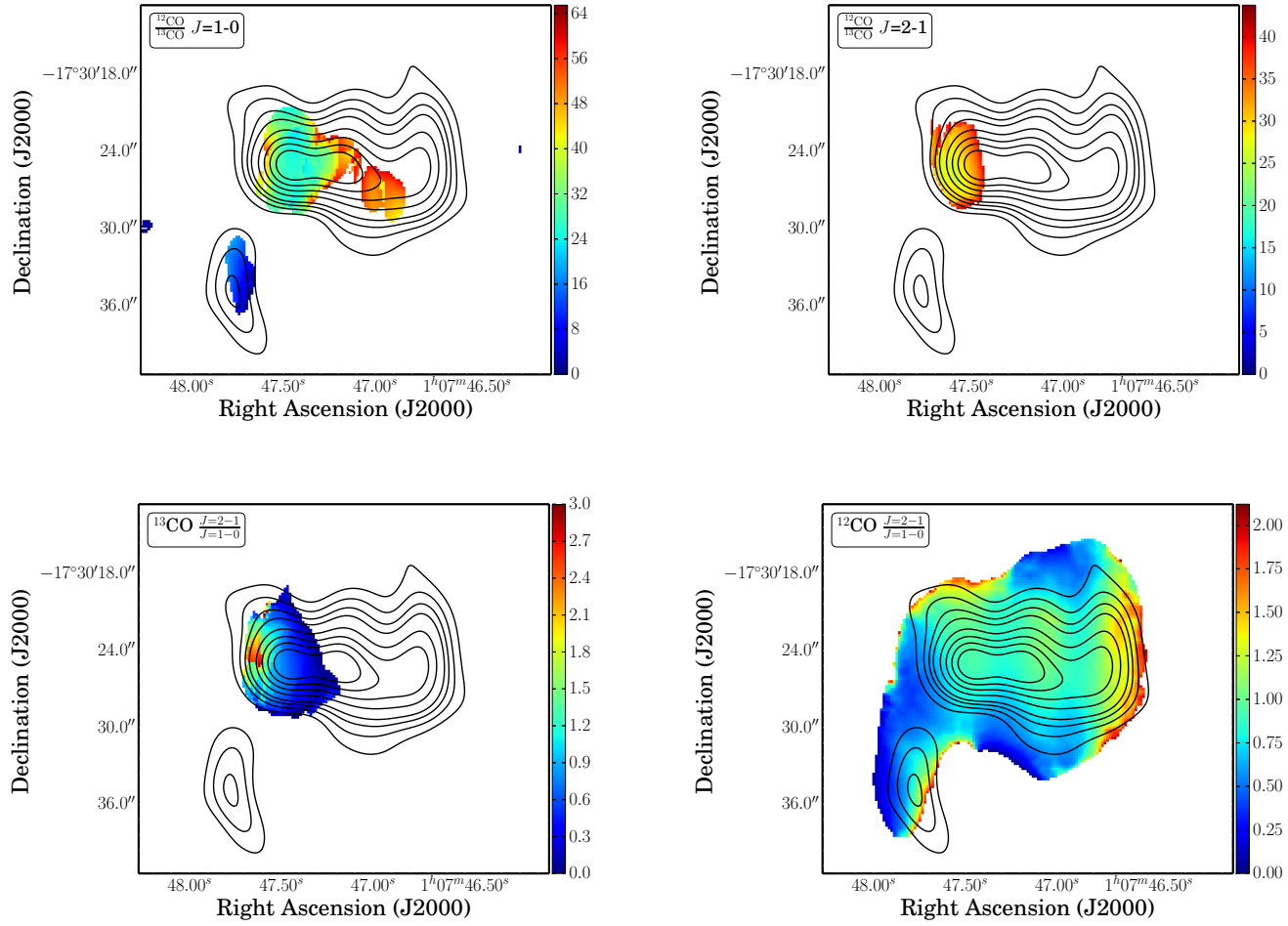
Figure 2.3 Line ratio maps: (*Top Left*) ^{13}CO $\frac{J=2-1}{J=1-0}$; (*Top Right*): $\frac{^{12}\text{CO}}{^{13}\text{CO}}$ J=2-1; (*Bottom Left*) $\frac{^{12}\text{CO}}{^{13}\text{CO}}$ J=1-0; (*Bottom Right*) ^{12}CO $\frac{J=2-1}{J=1-0}$. Only emission that is $> 3\sigma$ in both maps is included. Contours of ^{12}CO J=2-1 are shown to aid comparison between the maps.

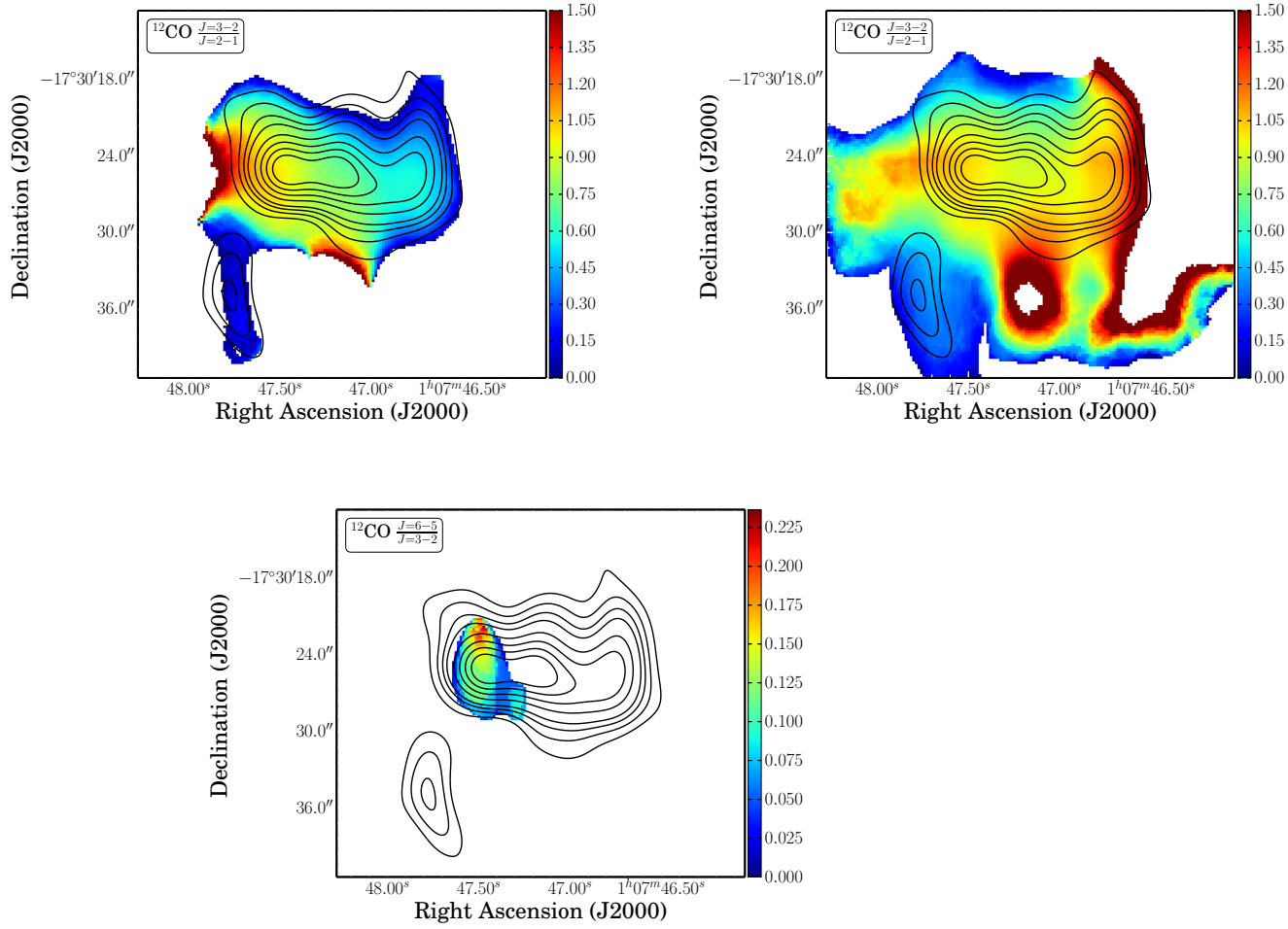Figure 2.4 Line ratio maps: (*Top Left*) SMA only ^{12}CO $\frac{J=3-2}{J=2-1}$; (*Top Right*): SMA + JCMT ^{12}CO $\frac{J=3-2}{J=2-1}$; (*Bottom*): ^{12}CO $\frac{J=6-5}{J=3-2}$. Contours and emission cutoffs as in Figure 3.
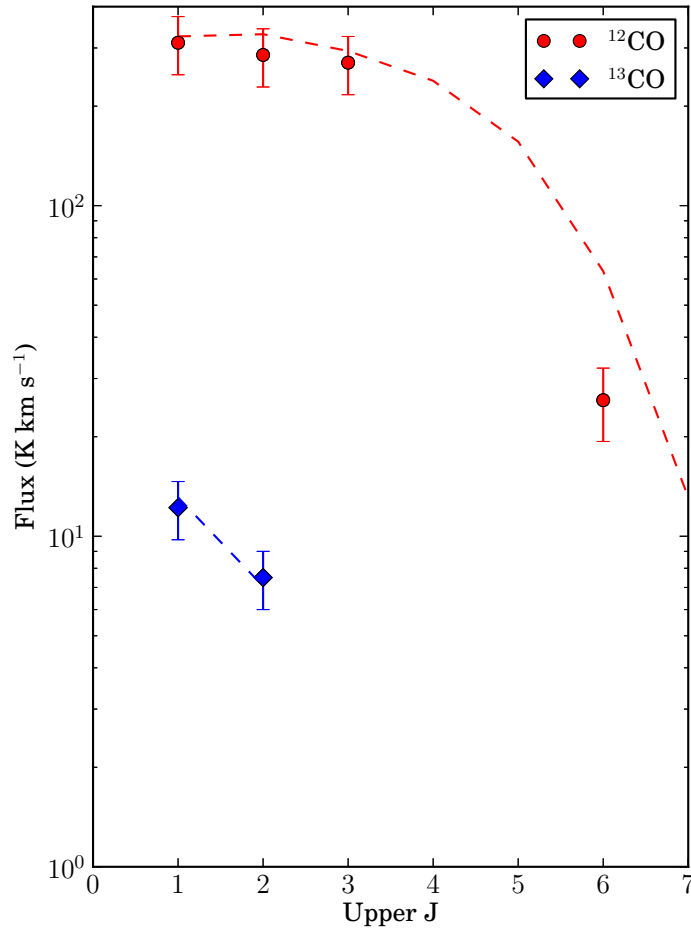
Figure 2.5 ^{12}CO (*red circles*) and ^{13}CO (*blue diamonds*) SLEDs of VV 114E using Grid 2 solutions. The dashed lines are the fitted SLEDs from the radiative transfer analysis.
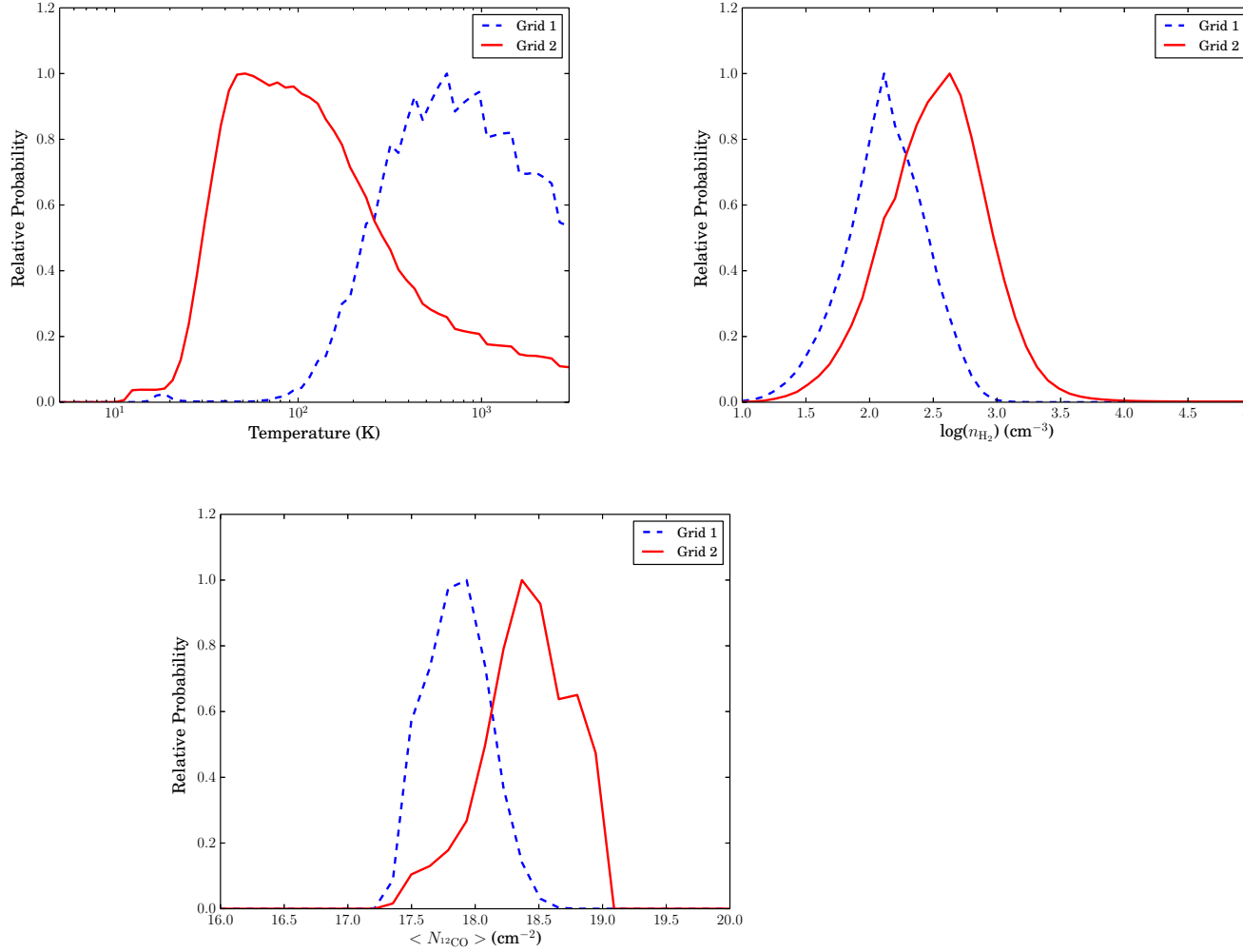
Figure 2.6 One-dimensional probability distributions for T_{kin} (top), n_{H_2} (middle) and $<N_{^{12}\text{CO}}>$ (bottom). Both Grid 1 and Grid 2 solutions are shown to display the difference in the solutions with differing $[^{12}\text{CO}]/[^{13}\text{CO}]$ values.

Figure 2.7 Two-dimensional distribution for T_{kin} vs. n_{H_2} using Grid 2 solutions. Diagonal lines indicate pressure in log $(K\ cm^{-3})$. Contour levels are 10%, 30%, 50%, 70% and 90% of the maximum likelihood.

Table 2.1.   Data For VV 114

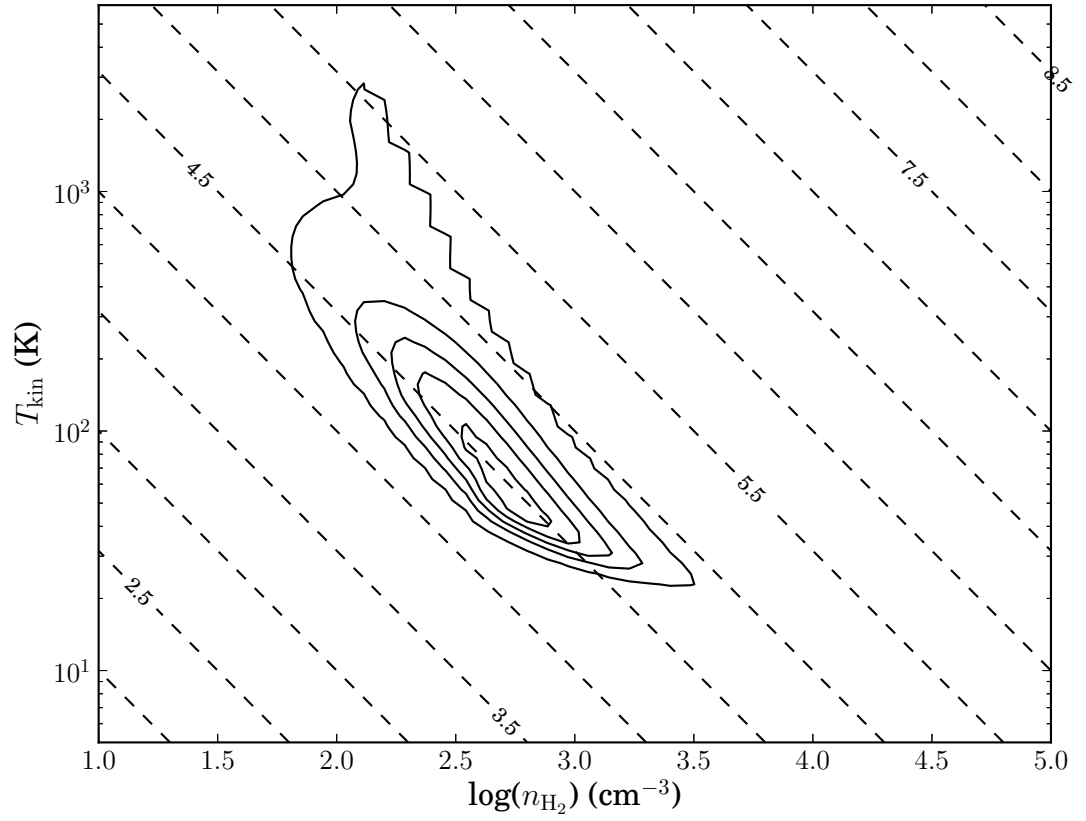| Transition Line	Interferometric Flux[a] (Jy km s^{-1})	JCMT Flux[a] (Jy km s^{-1})	JCMT + SMA Flux[a] (Jy km s^{-1})	Beam ($''$)	rms (mJy/be
^{12}CO J=1-0[c]	360 ± 20	-	-	6.5 × 3.7	25
^{12}CO J=2-1	1280 ± 50	2370 ± 60	2350 ± 70	4.0 × 3.0	13
^{12}CO J=3-2	1890 ± 60	4800 ± 200	4800 ± 60	2.8 × 2.0	25
^{12}CO J=6-5	150 ± 40	-	-	3.1 × 2.2	270
^{13}CO J=1-0[d]	4.0 ± 0.3	-	-	3.7 × 1.4	2
^{13}CO J=2-1	12.0 ± 2.0	-	-	4.6 × 3.4	10

[a]measurement uncertainty only; calibration uncertainty is 20% (Paper I).

[b]rms values for a 20 km s^{-1} channel width for all lines except ^{13}CO J=1-0 and ^{13}CO J=2-1 which 40 km s^{-1} and 50 km s^{-1} channel widths, respectively.

[c]OVRO map published in Yun et al. (1994)

[d]ALMA Cycle 0 map

Bibliography

Aalto, S., Booth, R. S., Black, J. H., & Johansson, L. E. B. 1995, A&A, 300, 369

Casoli, F., Dupraz, C., & Combes, F. 1992, A&A, 264, 55

Currie, M. J. et al. 2008, in Astronomical Society of the Pacific Conference Series, Vol. 394, Astronomical Data Analysis Software and Systems XVII, ed. R. W. Argyle, P. S. Bunclark, & J. R. Lewis, 650

Downes, D. & Solomon, P. M. 1998, ApJ, 507, 615

Frayer, D. T., Ivison, R. J., Smail, I., Yun, M. S., & Armus, L. 1999, AJ, 118, 139

Goldsmith, P. F. & Langer, W. D. 1978, ApJ, 222, 881

Greve, T. R., Papadopoulos, P. P., Gao, Y., & Radford, S. J. E. 2009, ApJ, 692, 1432

Harris, A. I. et al. 1991, ApJ, 382, L75

Henkel, C., Downes, D., Weiß, A., Riechers, D., & Walter, F. 2010, A&A, 516, A111

Ho, P. T. P., Moran, J. M., & Lo, K. Y. 2004, ApJ, 616, L1

Iono, D. et al. 2004, ApJ, 616, L63

—. 2009, ApJ, 695, 1537

—. 2013, PASJ, 65, L7

Kamenetzky, J. et al. 2011, ApJ, 731, 83

—. 2012, ApJ, 753, 70

Knop, R. A. et al. 1994, AJ, 107, 920

Langer, W. D. & Penzias, A. A. 1990, ApJ, 357, 477

Le Floc'h, E. et al. 2002, A&A, 391, 417

Maloney, P. R., Hollenbach, D. J., & Tielens, A. G. G. M. 1996, ApJ, 466, 561

Martín, S., Aladro, R., Martín-Pintado, J., & Mauersberger, R. 2010, A&A, 522, A62

Matsushita, S. et al. 2009, ApJ, 693, 56

Meijerink, R. et al. 2013, ApJ, 762, L16

Panuzzo, P. et al. 2010, A&A, 518, L37

Papadopoulos, P. P., van der Werf, P., Xilouris, E., Isaak, K. G., & Gao, Y. 2012, ApJ, 751, 10

Rangwala, N. et al. 2011, ApJ, 743, 94

Sanders, D. B., Mazzarella, J. M., Kim, D.-C., Surace, J. A., & Soifer, B. T. 2003, AJ, 126, 1607

Scoville, N. Z. et al. 2000, AJ, 119, 991

Sliwa, K. et al. 2012, ApJ, 753, 46

Stanimirovic, S. 1999, PhD thesis, Arecibo Observatory, NAIC/Cornell University

Stanimirovic, S. 2002, in Astronomical Society of the Pacific Conference Series, Vol. 278, Single-Dish Radio Astronomy: Techniques and Applications, ed. S. Stanimirovic, D. Altschuler, P. Goldsmith, & C. Salter, 375–396

U, V. et al. 2012, ApJS, 203, 9

van der Tak, F. F. S., Black, J. H., Schöier, F. L., Jansen, D. J., & van Dishoeck, E. F. 2007, A&A, 468, 627

Ward, J. S., Zmuidzinas, J., Harris, A. I., & Isaak, K. G. 2003, ApJ, 587, 171

Wilson, C. D., Walker, C. E., & Thornley, M. D. 1997, ApJ, 483, 210

Wilson, C. D. et al. 2008, ApJS, 178, 189

Wilson, T. L. & Rood, R. 1994, ARA&A, 32, 191

Yun, M. S., Scoville, N. Z., & Knop, R. A. 1994, ApJ, 430, L109

Chapter 3

Around the Ring We Go: The Cold, Dense Ring of Molecular Gas in NGC 1614

"Theories crumble, but good observations never fade."

HARLOW SHAPLEY (1885 - 1972)

3.1   Introduction

High-resolution observations of molecular gas in nearby luminous infrared galaxies (LIRGs) reveal concentrations of gas near the nuclei of the merging galaxies (e.g. Downes & Solomon 1998, Wilson et al. 2008). Tidal interactions of gas-rich galaxies are largely responsible for funnelling the molecular gas to the central kiloparsec, compressing the gas which, in turn, triggers a starburst (e.g. Mihos & Hernquist 1996). Even minor mergers between a gas-rich galaxy and a satellite companion can be efficient at driving molecular gas towards the

central regions (e.g. Mihos & Hernquist 1994).

NGC 1614 ($D_L = 67.9$ Mpc; $1'' = 330$ pc) has a far-infrared luminosity (L_{FIR}) of 2.7×10^{11} $L_\odot$ (Sanders et al. 2003). Optically, this galaxy has a bright center and two fairly symmetric inner spiral arms (Neff et al., 1990). A circumnuclear ring is seen in several tracers, such as Paα (Alonso-Herrero et al., 2001), radio continuum (Olsson et al., 2010), PAHs (Väisänen et al., 2012) and ^{12}CO J=2-1 (König et al., 2013). The ring hosts a very young starburst (5-10 Myr), while the nucleus hosts an older starburst (>10 Myr; Olsson et al. 2010). Using the Atacama Large Millimeter/submillimeter Array (ALMA), Imanishi & Nakanishi (2013) observed the dense gas tracers HCN/HCO$^+$/HNC J=4-3 which showed emission that was consistent with starburst-dominated galaxies. Numerical simulations of NGC 1614 suggest a minor merger with the primary galaxy being 3-5 times more massive (Väisänen et al., 2012).

In this Letter, we present unpublished archival ALMA and new CARMA CO observations for NGC 1614. We combine the new observations with previously published Submillimeter Array (SMA) observations to constrain the physical conditions in the molecular gas using a radiative transfer code and a Bayesian likelihood method. In Section 2, we describe the observations and line ratio maps. In Section 3, we discuss the morphology of NGC 1614 seen in the new observations. In Section 4, we present the results of the radiative transfer analysis, compare them to other LIRGs and discuss the ^{12}CO-to-^{13}CO abundance ratio, [^{12}CO]/[^{13}CO]. In Section 5, we discuss the CO-to-H$_2$ conversion factor, α_{CO} and put limits on the ^{12}CO-to-H$_2$ abundance ratio, x_{CO}.

3.2   Observations

We use high-resolution observations from CARMA, SMA and ALMA to constrain the physical conditions of the molecular gas (see Table 1 for details). The calibration methods are outlined in the following sections. All datasets have been continuum subtracted using line-free channels and imported into CASA for further processing and imaging. We created datacubes with 20 km s^{-1} and 100 km s^{-1} channel widths for ^{12}CO and ^{13}CO, respectively. Integrated intensity maps (Figure 1) were created using channels with line emission and all integrated intensity maps have been primary beam corrected.

3.2.1   CARMA

NGC 1614 was observed using CARMA in the C-array configuration on 2012 December 03 and 18 and D-array configuration on 2012 November 14, 18 and 20 in ^{12}CO and ^{13}CO J=1-0, simultaneously. We use CASA to calibrate and image the uv-datasets. The flux calibrator was Uranus and the bandpass and gain calibrator was 0423-013. We combine both array configurations into one dataset for imaging.

3.2.2   SMA

NGC 1614 was observed with the SMA in ^{12}CO and ^{13}CO J=2-1 and ^{12}CO J=3-2 using the compact array configuration (Wilson et al. 2008). The data processing is described in Wilson et al. (2008). NGC 1614 was also observed with the SMA using the extended and very-extended (König et al., 2013) array configurations in ^{12}CO and ^{13}CO J=2-1. We obtained the raw data for the extended observations and the calibrated data for the very-extended observations

from the SMA archive. We calibrated the extended configuration data using CASA. Uranus, 3C454.3 and 0423-013 were used as the flux, bandpass and gain calibrators, respectively. We combined data from all three configurations to obtain high-resolution maps of ^{12}CO and ^{13}CO J=2-1.

To recover the short spacings of the SMA ^{12}CO J=2-1 and J=3-2 maps, we used the James Clerk Maxwell Telescope (JCMT) to map NGC 1614 in ^{12}CO J=2-1 using the RxA3 receiver on 2012 November 26 and 27 (Program: M12BC14; PI: K. Sliwa) and in ^{12}CO J=3-2 using the RxB3 receiver (Wilson et al. 2008). The reduction of the ^{12}CO J=3-2 JCMT map is described in Wilson et al. (2008). The ^{12}CO J=2-1 map covered 49″ on each side with a 21″ beam, ensuring we included all emission from NGC 1614. We created a continuum subtracted datacube with a velocity resolution of 20 km s^{-1} using the `Starlink` software (Currie et al. 2008). We assume a main beam efficiency (η_{mb}) of 0.6 for ^{12}CO J=3-2 and 0.69 for ^{12}CO J=2-1 to convert the antenna temperature units to main beam temperature (T_{mb}). We convert the T_{mb} units to Jy km s^{-1} using the scaling factors of 26.9 Jy K$(T_{mb})^{-1}$ and 22.9 Jy K$(T_{mb})^{-1}$ for ^{12}CO J=3-2 and J=2-1, respectively. We combined the JCMT and SMA data using the "feathering" method as described in Sliwa et al. (2012).

3.2.3   ALMA

NGC 1614 was observed in ^{12}CO J=3-2 and ^{12}CO J=6-5 using ALMA during Cycle 0. We use the calibrated uv-datasets obtained from the ALMA archive. We performed two rounds of phase-only self-calibration on both datasets using the ^{12}CO line emission. When imaging the ^{12}CO J=3-2 ALMA data, we use the SMA short-spacings recovered ^{12}CO J=3-2 datacube as a starting model

so as to better constrain the shorter baselines. The flux scales of the two datasets differ by roughly 10%; however, this is within our assumed calibration uncertainty of 20%. Along with ^{12}CO J=3-2, HCO$^+$ J=4$-$3 was observed simultaneously in the upper sideband. We present the integrated intensity map in Figure 1, but do not include the line in our analysis. **We also create three 435μm$_{rest}$ continuum maps using the upper sideband (USB), lower sideband (LSB) and both sidebands. Each sideband is roughly 4GHz in width. All three maps are consistent in flux and structure.**

3.2.4 Line Ratios

We created the following line ratio maps: r_{21} = ^{12}CO (J=2-1/J=1-0), r_{32} = ^{12}CO(J=3-2/J=2-1), r_{63} = ^{12}CO(J=6-5/J=3-2), $^{13}r_{21}$ = ^{13}CO(J=2-1/J=1-0), R_{10} = ^{12}CO/^{13}CO J=1-0, R_{21} = ^{12}CO/^{13}CO J=2-1, H_{43} = HCO$^+$ J=4$-$3/^{12}CO J=3-2 and H_{46} = HCO$^+$ J=4$-$3/^{12}CO J=6-5. We match the angular resolutions of the two maps used to create the individual line ratio maps (Figure 2). We implemented a 3σ cutoff on each map except ^{13}CO J=2-1, where a 1σ cutoff was used. The r_{21}, r_{32} and r_{63} maps show that within the central ring region, the line ratios vary smoothly with no significant changes until the outer regions of the ring where the line ratios drop. As is normal for LIRGs, the R_{10} and R_{21} line ratios are unusually high when compared to normal disk galaxies.

3.3 Morphology

Our CARMA ^{12}CO J=1-0 observations do not resolve the ring structure, instead showing a single compact nucleus. **The highest resolution**

map of the OVRO ^{12}CO J=1-0 observations of Olsson et al. (2010) is at a slightly better resolution and shows an elongated structure; however, our CARMA observations do show a slight extension to the east. Our CARMA observations recover roughly 3 times more flux than the lower resolution map of Olsson et al. (2010), which may be due to a difference in sensitivity **and uv-coverage.**

The SMA and ALMA data resolve the previously observed ring structure within NGC 1614. The SMA+JCMT ^{12}CO J=2-1 and ALMA+SMA ^{12}CO J=3-2 maps show extended structure to the east and to the southwest beyond the ring of molecular gas. The extended structure in the high-resolution maps is due to an increase in sensitivity of the maps and also the inclusion of short baselines. Overlaying the high-resolution ^{12}CO J=3-2 map on an optical HST image shows that the eastern structure runs along the dust lanes in the southeastern spiral arm, while the southwestern structure extends into the dust features to the west (Figure 1 **bottom middle**). This suggests that the gas and dust are associated and well mixed together.

The ALMA ^{12}CO J=6-5 observations are the first of their kind for NGC 1614. The ring structure is also seen in ^{12}CO J=6-5 and 435 μm_{rest} continuum; however, the extended features seen in ^{12}CO J=2-1 and J=3-2 are not detected. The lack of detection suggests that the molecular gas outside of the ring is more diffuse with physical conditions that favour the low-J CO transitions. In addition, any ^{12}CO J=6-5 emission outside the ring will come from diffuse structures that are filtered out at high resolutions with ALMA. Finally, we measure a total ^{12}CO J=6-5 flux of 1320 $\pm$ 40 Jy km s^{-1} from the Herschel FTS spectrum of NGC 1614. This shows that the ALMA map is missing roughly 30% of the ^{12}CO J=6-5 flux which may well reside in a diffuse

structure.

3.4   Molecular Gas Physical Conditions

To constrain the physical conditions of the molecular gas, we use the radiative transfer code RADEX (van der Tak et al. 2007). For ^{12}CO, we create a grid of temperature (T_{kin}; range=$10^{0.7}$-$10^{3.8}$ K, 71 points), density ($n_{\mathrm{H_2}}$; range=$10^{1.0}$-$10^{7.0}$ cm^{-3}, 71 points), column density ($N_{^{12}\mathrm{CO}}$; range=$10^{12.0}$-$10^{22.0}$ cm^{-2}, 81 points) and filling factor (Φ_{A}; range=10^{-5}-1, 71 points). For ^{13}CO, we create a similar grid with a wide range of ^{12}CO-to-^{13}CO abundance ratios ([^{12}CO]/[^{13}CO]; range=10-10^5, 51 points).

In addition to the RADEX grids, we use a Bayesian likelihood code to create probability distributions for the various parameters. Two calculated values are presented for each parameter: 1DMax and 4DMax. The 1DMax is the maximum likelihood of a specific parameter from the one-dimensional distribution for that parameter. The 4DMax is the maximum likelihood of a single grid point based on the four-dimensional distribution of the parameters that comprise the grid. For more details on the likelihood code, see Kamenetzky et al. (2012). We also implemented the three priors described in Sliwa et al. (2013).

We focus our analysis on the central ring structure because outside the ring the missing flux is seen to be >20%, our assumed calibration uncertainty, in our short spacing recovered ^{12}CO J=2-1 and J=3-2 maps . We model the physical conditions at a resolution of **0.7″×0.6″ (230 pc × 200 pc)** at the five peak intensity positions (Figure 1) around the ring: **north (α_{J2000} = 04^{h}34^{m}00^s.000, δ_{J2000} = -08°34′44″.251), south**

($\alpha_{J2000} = \mathbf{04^h34^m00^s.020}$, $\delta_{J2000} = \mathbf{-08°34'45''.844}$), **east** ($\alpha_{J2000} = \mathbf{04^h34^m00^s.080}$, $\delta_{J2000} = \mathbf{-08°34'45''.006}$), **west** ($\alpha_{J2000} = \mathbf{04^h33^m59^s.980}$, $\delta_{J2000} = \mathbf{-08°34'45''.064}$) **and the "hole"** ($\alpha_{J2000} = \mathbf{04^h34^m00^s.027}$, $\delta_{J2000} = \mathbf{-08°34'45''.075}$). Since we do not have high-resolution ^{12}CO and ^{13}CO J=1-0 observations and ^{13}CO J=2-1 is not detected at all positions in the ring, we adopt the following line ratios to estimate the flux for these three lines at each position of the ring: $r_{21} = 0.93 \pm 0.23$, $^{13}r_{21} = 2.0 \pm 0.6$, and $R_{21} = 20 \pm 3$. These line ratios, within uncertainty, span the observed values and the line ratios across the ring do not vary dramatically.

Over the ring the results are quite consistent and reveal a cold (T_{kin}=20-40K), dense ($n_{\mathrm{H_2}} > 10^{3.0}$ cm^{-3}) molecular gas component (Table 2, Figure 3). Interestingly, only the "hole" shows evidence of a second warmer molecular gas component; it is not possible to fit all four ^{12}CO lines with a single component (Figure 3). We re-model the molecular gas of the "hole" excluding the ^{12}CO J=6-5 flux. The lower-J lines are better fit without ^{12}CO J=6-5 revealing again, cold, dense molecular gas. More higher-J CO observations would be required to constrain the properties of the warmer component in NGC 1614. For the other regions, the cold molecular gas component is dominant but it does not rule out a second warmer component as seen with the Antennae (Schirm et al. 2014), Arp 220 (Rangwala et al. 2011) and M82 (Kamenetzky et al. 2012).

The molecular gas in Arp 299 (Sliwa et al. 2012) and the Antennae (Schirm et al. 2014) is similar to the molecular gas in the ring which could suggest that NGC 1614 is at a similar merger stage to these two LIRGs. This is consistent with age estimates using numerical modeling, which suggest that NGC1614 is ∼50 Myr after the second passage (Väisänen et al., 2012) and

the Antennae is at a similar stage (Privon et al. 2013). **In contrast, the molecular gas of the late stage mergers VV114 (Sliwa et al. 2013) and Arp220 (Matsushita et al. 2009) is more diffuse ($< 10^{3.0}$ cm^{-3}) and warmer ($<$30K), respectively. Note that all these analyses differ in their physical resolutions.**

Sliwa et al. (2013) showed that the [^{12}CO]/[^{13}CO] ratio for the LIRG VV 114 is roughly 3 larger than in the local ISM. For NGC 1614, we see similar results for [^{12}CO]/[^{13}CO], where the maximum likelihood value exceeds 130 around the ring. The "hole" has a much lower most probable [^{12}CO]/[^{13}CO] value, similar to the value for the inner regions of the Galaxy (Langer& Penzias 1990). In the Galaxy, [^{12}CO]/[^{13}CO] increases with increasing radius. During the merger process, molecular gas can be driven towards the central regions, which can bring in high [^{12}CO]/[^{13}CO] valued molecular gas and drive up the [^{12}CO]/[^{13}CO] ratio (Casoli et al. 1992). Since the "hole" has a maximum likelihood [^{12}CO]/[^{13}CO] value much lower than the ring, this implies that the infalling molecular gas has not reached the "hole" and supports the idea of a resonance phenomenon slowing down the infall of molecular gas at certain radii (König et al., 2013).

3.5 CO-to-H$_2$ Conversion Factor

Narayanan et al. (2011) found that the combination of increased velocity dispersion and T_{kin} increases the CO intensity, and thus lowers the ^{12}CO luminosity to H$_2$ mass conversion factor, α_{CO} (=M$_{H_2}$/L$_{CO}$), by $\sim$2-10 times from the Galactic value ($\alpha_{CO;Galactic} = 4.3$ $M_\odot$ (K km s^{-1} pc^2)$^{-1}$; Bolatto, Wolfire

& Leory 2013) in mergers. We measure α_{CO} using the following

$$\alpha_{CO} = \frac{N_{^{12}CO} \cdot \text{area} \cdot m_{H_2}}{M_\odot \cdot x_{CO}} \frac{r_{21}}{L_{COJ=2-1}} \qquad (3.1)$$

where $N_{^{12}\text{CO}}$ is the 4DMax column density, area is calculated from the beam size, m_{H_2} is the mass of molecular hydrogen, x_{CO} is the CO-to-H_2 abundance ratio assumed to be 3×10^{-4} (Ward et al. 2003) and $L_{COJ=2-1}$ is the ^{12}CO J=2-1 luminosity in K km s^{-1} pc^2. We use the line ratio r_{21}=0.93 $\pm$ 0.23 to estimate the ^{12}CO J=1-0 luminosity from the ^{12}CO J=2-1 luminosity at $\sim 0.7''$ (230pc) resolution. Around the ring, α_{CO} varies from 0.9 - 1.5 $(\frac{3\times 10^{-4}}{x_{\text{co}}})M_\odot(\text{K km s}^{-1} \text{ pc}^2)^{-1}$ (Table 2). The "hole" has a measured α_{CO} that is nearly an order of magnitude lower.

The ring of NGC 1614 has intermediate α_{CO} values when compared to other LIRGs such as Arp 299 (0.4 $M_\odot$ (K km s^{-1} pc^2)$^{-1}$; Sliwa et al. 2012) and VV 114 (0.5 $M_\odot$ (K km s^{-1} pc^2)$^{-1}$; Sliwa et al. 2013). The Antennae was measured to have an α_{CO} of ~ 7 $M_\odot$ (K km s^{-1} pc^2)$^{-1}$ on **a 390 pc scale (Wilson et al. 2003)**. The difference in α_{CO} value between the Antennae and NGC 1614 could suggest two scenarios: the transition from a Galactic-like value to a ULIRG-like value (Downes & Solomon 1998) is extremely rapid or the Antennae has yet to hit its peak star formation rate. Narayanan et al. (2011) showed that during the merger process, α_{CO} drops to its lowest value around the star formation peak. The star formation rate of the Antennae is nearly an order of magnitude lower than that of NGC 1614.

The biggest uncertainty in measuring α_{CO} is the assumed value of x_{CO}. Clouds in Taurus and ρ Ophiuchi have a measured value of $x_{\text{CO}} = 8.5 \times 10^{-5}$ (Frerking, Langer & Wilson 1982), while the ratio measured in warm, star

forming clouds can be higher, such as NGC 2024 with a measured $x_{\rm CO}$ of 2.7 $\times\ 10^{-4}$ (Lacy et al. 1994). Since NGC 1614 is undergoing a starburst (SFR $\sim 52\ M_\odot\ {\rm yr}^{-1}$; U et al. 2012), we assume a high $x_{\rm CO}$ value, similar to that of NGC 2024. The "hole" in the molecular ring, however, is not forming stars vigorously and the molecular gas is colder; therefore, the $x_{\rm CO}$ that we have adopted may not be appropriate for the "hole". If $x_{\rm CO}$ is lower in the "hole", this would drive up the measured α_{CO} value.

Schirm et al. (2014) found an $x_{\rm CO}$ of 5×10^{-5} for the Antennae by comparing their hot molecular gas mass to that derived using *Spitzer* H_2 vibrational transitions. We are unable to perform such an analysis for NGC 1614 due to the lack of high-J CO observations; however, we can place lower limits on $x_{\rm CO}$ using the dynamical masses (M_{dyn}) of the regions around the ring. We measure M_{dyn} using the line width and the source size, both measured using the ^{12}CO J=3-2 map. We then use M_{dyn} and the CO luminosity within the region to measure $\alpha_{CO,dyn}$ ($=M_{dyn}/{\rm L}_{CO}$). Since M_{dyn} is the mass of all matter (i.e. stars, gas, dust, and dark matter), $\alpha_{CO,dyn}$ is an upper limit,

$$\alpha_{CO,dyn} \geq \alpha_{CO,true} \propto \frac{1}{x_{CO}} \qquad (3.2)$$

In addition, the measured M_{dyn} is only valid for regions that are gravitationally bound; however, given their size, our regions are likely not gravitationally bound and so the measured M_{dyn} is itself also an upper limit. For the east, west and south regions, we measure $\alpha_{CO,dyn}$ to be 3.5, 2.6 and 2.4 $M_\odot$ (K km s^{-1} pc^2)$^{-1}$, respectively. This sets a lower limit on $x_{\rm CO}$ of 1.1-1.4 $\times\ 10^{-4}$. For the north region, we get an interesting result: $\alpha_{CO,dyn}$ is exactly what we measured from the radiative transfer analysis. This implies that our assumption of $x_{\rm CO}$

for the north region is likely not valid and should be higher by some factor which would drive α_{CO} to lower values. If we assume that the ratio between the M_{dyn} and radiative transfer α_{CO} is similar for all regions around the ring (excluding the "hole"), x_{CO} should be $\sim$2-3 times larger than our assumption of 3×10^{-4} driving the value from 1.2 $M_{\odot}$ (K km s^{-1} pc^2)$^{-1}$ to 0.4-0.6 $M_{\odot}$ (K km s^{-1} pc^2)$^{-1}$.

One thing is certain about α_{CO} for NGC 1614: the Galactic value does not apply and a more ULIRG-type value should be used to measure the amount of molecular gas. With future ALMA observations of other high-J CO lines and James Webb Space Telescope observations of vibrational H$_2$ transitions in the near-infrared, we will be able to put better constraints on x_{CO} and in turn α_{CO} for NGC 1614.

Bibliography

Alonso-Herrero, A., Engelbracht, C. W., Rieke, M. J., Rieke, G. H., & Quillen, A. C. 2001, ApJ, 546, 952

Bolatto, A. D., Wolfire, M., & Leroy, A. K. 2013, ARA&A, 51, 207

Casoli, F., Dupraz, C., & Combes, F. 1992, A&A, 264, 55

Currie, M. J., Draper, P. W., Berry, D. S., Jenness, T., Cavanagh, B., et al. 2008, in Astronomical Society of the Pacific Conference Series, Vol. 394, Astronomical Data Analysis Software and Systems XVII, ed. R. W. Argyle, P. S. Bunclark, & J. R. Lewis, 650

Downes, D. & Solomon, P. M. 1998, ApJ, 507, 615

Frerking, M. A., Langer, W. D., & Wilson, R. W. 1982, ApJ, 262, 590

Imanishi, M. & Nakanishi, K. 2013, AJ, 146, 47

Kamenetzky, J., Glenn, J., Rangwala, N., Maloney, P., Bradford, M., et al. 2012, ApJ, 753, 70

König, S., Aalto, S., Muller, S., Beswick, R. J., & Gallagher, J. S. 2013, A&A, 553, A72

Lacy, J. H., Knacke, R., Geballe, T. R., & Tokunaga, A. T. 1994, ApJ, 428, L69

Langer, W. D. & Penzias, A. A. 1990, ApJ, 357, 477

Matsushita, S., Iono, D., Petitpas, G. R., Chou, R. C.-Y., Gurwell, M. A., et al. 2009, ApJ, 693, 56

Mihos, J. C. & Hernquist, L. 1994, ApJ, 425, L13

—. 1996, ApJ, 464, 641

Narayanan, D., Krumholz, M., Ostriker, E. C., & Hernquist, L. 2011, MNRAS, 418, 664

Neff, S. G., Hutchings, J. B., Standord, S. A., & Unger, S. W. 1990, AJ, 99, 1088

Olsson, E., Aalto, S., Thomasson, M., & Beswick, R. 2010, A&A, 513, A11

Privon, G. C., Barnes, J. E., Evans, A. S., Hibbard, J. E., Yun, M. S., et al. 2013, ApJ, 771, 120

Sanders, D. B., Mazzarella, J. M., Kim, D.-C., Surace, J. A., & Soifer, B. T. 2003, AJ, 126, 1607

Schirm, M. R. P., Wilson, C. D., Parkin, T. J., Kamenetzky, J., Glenn, J., et al. 2014, ApJ, 781, 101

Sliwa, K., Wilson, C. D., Krips, M., Petitpas, G. R., Iono, D., et al. 2013, ApJ, 777, 126

Sliwa, K., Wilson, C. D., Petitpas, G. R., Armus, L., Juvela, M., et al. 2012, ApJ, 753, 46

U, V., Sanders, D. B., Mazzarella, J. M., Evans, A. S., Howell, J. H., et al. 2012, ApJS, 203, 9

Väisänen, P., Rajpaul, V., Zijlstra, A. A., Reunanen, J., & Kotilainen, J. 2012, MNRAS, 420, 2209

van der Tak, F. F. S., Black, J. H., Schöier, F. L., Jansen, D. J., & van Dishoeck, E. F. 2007, A&A, 468, 627

Ward, J. S., Zmuidzinas, J., Harris, A. I., & Isaak, K. G. 2003, ApJ, 587, 171

Wilson, C. D., Petitpas, G. R., Iono, D., Baker, A. J., Peck, A. B., et al. 2008, ApJS, 178, 189

Wilson, C. D., Scoville, N., Madden, S. C., & Charmandaris, V. 2003, ApJ, 599, 1049

Table 3.1.   Data for NGC 1614

Transition Line	Observatory	Interferometric Flux[a] (Jy km s^{-1})	Resolution ($''$)	rms [b] (mJy beam$^-$)
^{12}CO J=1-0	CARMA	240 ± 14	3.3 x 2.9	4
^{12}CO J=2-1	SMA	1250 ± 5	0.7 x 0.6	7.5
^{12}CO J=3-2	SMA	1160 ± 80	2.7 x 2.2	43
^{12}CO J=3-2	ALMA	1680 ± 10	0.7 x 0.4	3
^{12}CO J=6-5	ALMA	920 ± 10	0.4 x 0.3	7
HCO$^+$ J=4$-$3	ALMA	24.3 ± 0.6	0.6×0.4	0.9
^{13}CO J=1-0	CARMA	3.6 ± 0.5	3.8 x 3.2	3.1
^{13}CO J=2-1	SMA	16.0 ± 0.5	0.8 x 0.7	3.3
Continuum (435μm$_{rest}$)	ALMA	240 ± 4 (mJy)	0.3 x 0.2	1.4^c

[a]Measurement uncertainty only. Calibration uncertainty is 20% for all maps.

[b]Velocity channel widths of 20 km s^{-1} for ^{12}CO and HCO$^+$ maps and 100 km s^{-1} for ^{13}CO maps.

[b]Noise level determined using the combined USB and LSB map.

Table 3.2.   Modelling Results

| Region		$T_{\rm kin}$ (K)	$n_{\rm H_2}$ (cm^{-3})	Pressure (K cm^{-3})	$<N_{^{12}\rm CO}>$ (cm^{-2})	Mass ($M_\odot$)	[^{12}CO]/[^{13}CO]	α_{CO} ($M_\odot$ (K km s^{-1} pc^2)
North	1DMax	25	$10^{4.00}$	$10^{5.47}$	$10^{18.87}$	$10^{7.33}$	131	1.2
	4DMax	31	$10^{3.83}$	$10^{5.47}$	$10^{18.87}$	$10^{7.33}$	131	1.2
	1σ range	21-64	$10^{2.98}$-$10^{5.67}$	$10^{5.05}$-$10^{7.11}$	$10^{18.44}$-$10^{19.27}$	$10^{6.90}$-$10^{7.73}$	83-575	-
West	1DMax	23	$10^{4.17}$	$10^{5.86}$	$10^{19.51}$	$10^{7.98}$	575	1.2
	4DMax	34	$10^{3.74}$	$10^{5.86}$	$10^{19.51}$	$10^{7.98}$	575	1.2
	1σ range	20-41	$10^{3.90}$-$10^{6.37}$	$10^{5.43}$-$10^{7.85}$	$10^{18.53}$-$10^{19.47}$	$10^{6.99}$-$10^{7.93}$	104-954	-
South	1DMax	23	$10^{4.17}$	$10^{5.86}$	$10^{19.36}$	$10^{7.82}$	575	0.9
	4DMax	34	$10^{3.83}$	$10^{5.86}$	$10^{19.36}$	$10^{7.82}$	575	0.9
	1σ range	19-39	$10^{3.90}$-$10^{6.39}$	$10^{5.43}$-$10^{7.83}$	$10^{18.47}$-$10^{19.44}$	$10^{6.93}$-$10^{7.90}$	102-1020	-
East	1DMax	25	$10^{7.00}$	$10^{8.28}$	$10^{19.36}$	$10^{7.82}$	691	1.5
	4DMax	42	$10^{3.74}$	$10^{8.28}$	$10^{19.36}$	$10^{7.82}$	691	1.5
	1σ range	20-41	$10^{4.18}$-$10^{6.49}$	$10^{5.76}$-$10^{8.02}$	$10^{18.45}$-$10^{19.32}$	$10^{6.92}$-$10^{7.78}$	148-1122	-
Hole	1DMax	11	$10^{3.74}$	$10^{4.96}$	$10^{17.98}$	$10^{6.44}$	52	0.1
	4DMax	15	$10^{3.91}$	$10^{4.96}$	$10^{17.98}$	$10^{6.44}$	52	0.1
	1σ range	10-59	$10^{3.04}$-$10^{6.16}$	$10^{4.77}$-$10^{7.43}$	$10^{17.72}$-$10^{18.90}$	$10^{6.19}$-$10^{7.36}$	42-489	-
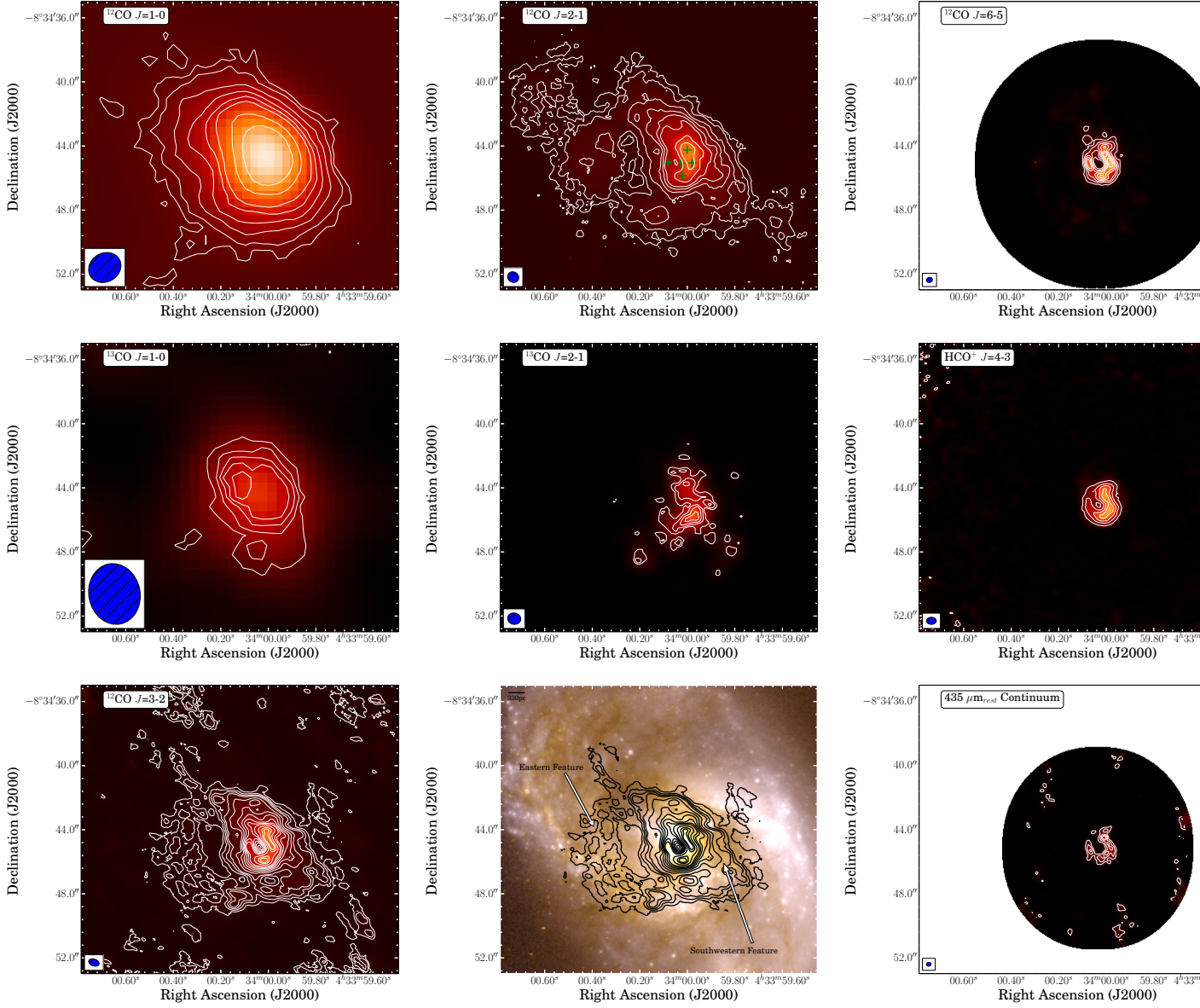
Figure 3.1 Integrated intensity maps for NGC 1614. **Ellipses in the lower left corner indicate the beam resolution.** *Top Row:* (Left) CARMA ^{12}CO J=1-0 map. Contours correspond to $(1,2,4,6,8,10,15,20) \times 1.03$ Jy beam^{-1} km s^{-1}. (Middle) SMA+JCMT ^{12}CO J=2-1 map. **Green crosses represent the positions of radiative transfer analysis.** Contours correspond to $(1,2,4,6,8,10,15,20,30) \times 1.37$ Jy beam^{-1} km s^{-1}. (Right) ALMA ^{12}CO J=6-5 map. Contours correspond to $(5,10,15,20,25,30) \times 1.26$ Jy beam^{-1} km s^{-1}. *Middle Row:* (Left) CARMA ^{13}CO J=1-0 map. Contours correspond to $(1,1.5,2,2.5,3) \times 0.62$ Jy beam^{-1} km s^{-1}. (Middle) SMA ^{13}CO J=2-1 map. Contours correspond to $(0.5,1,1.5,2,2.5,3) \times 1.0$ Jy beam^{-1} km s^{-1}. (Right) ALMA HCO$^+$ J=4−3 map. Contours correspond to $(3,6,9,12,15) \times 0.168$ Jy beam^{-1} km s^{-1}. *Bottom Row:* (Left) ALMA+SMA ^{12}CO J=3-2 map. Contours correspond to $(4,6,8,10,15,20,25,30,35,40,50,60,65) \times 0.64$ Jy beam^{-1} km s^{-1}. (Middle) ALMA+SMA ^{12}CO J=3-2 contours overlaid on HST 814/435 color map. (Right): ALMA 435 μm$_{rest}$ continuum created with both sidebands. Contours correspond to $(3,6,9,12) \times 0.0014$ Jy beam^{-1}.
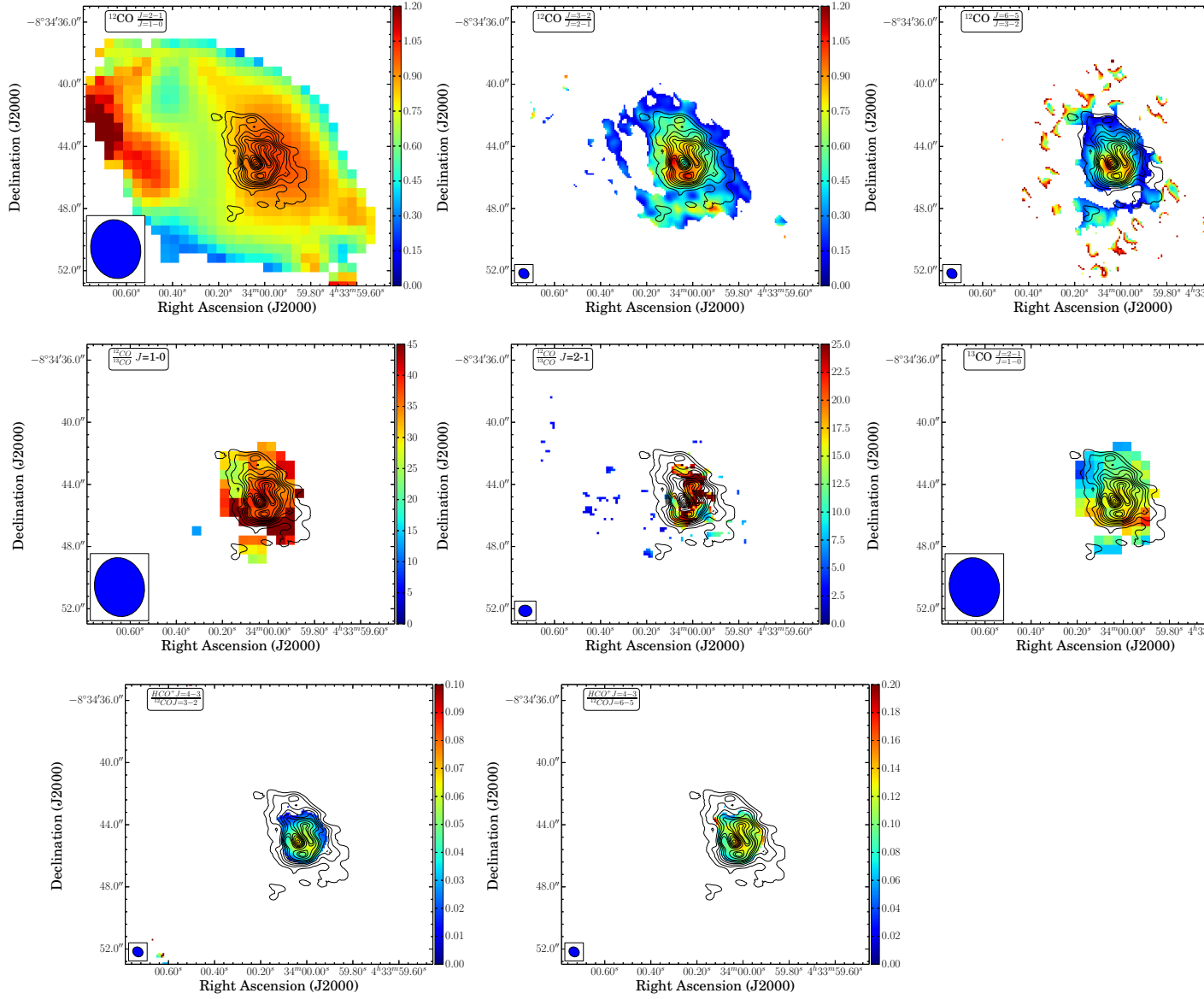
Figure 3.2 Line ratio maps. Contours correspond to ^{12}CO J=3-2 from Figure 1 starting at 10×0.64 Jy beam^{-1} km s^{-1}. *Top Row: r_{21}, r_{32} and r_{63} Middle Row: R_{10}, R_{21} and $^{13}r_{21}$ Bottom Row: H_{43} and H_{46}.*
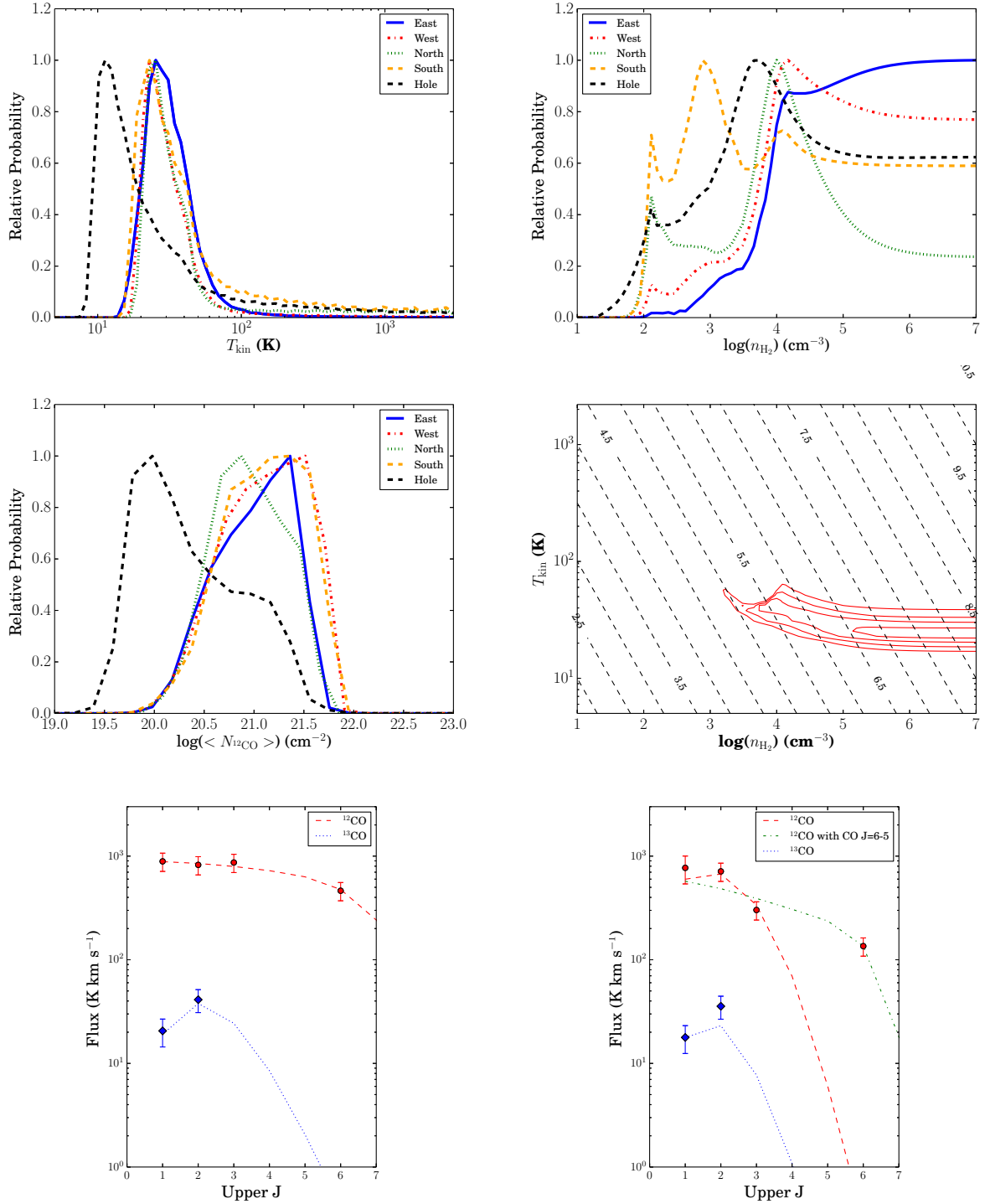
Figure 3.3 *Top Row:* (Left) Probability distribution of $T_{\rm kin}$. (Right) Probability distribution of $\log(n_{\rm H_2})$. *Middle Row:* (Left) Probability distribution of $\log(<N_{\rm ^{12}CO}>)$. (Right) Sample probability contour plot of $T_{\rm kin}$ versus $\log(n_{\rm H_2})$ for the eastern region. Solid contours represent $(30,50,70,90)\%$ of the maximum probable solution. Dashed contours represented pressure. *Bottom Row:* (Left) Example spectral line energy distribution (SLED) for the eastern region of NGC 1614. Dashed lines represent the 4DMax solution. (Right) CO SLED for the "hole". Green dashed lines represent the 4DMax solution that includes the ^{12}CO $J=6-5$ flux into the modelling.

Chapter 4

Around the Ring We Go: The Cold, Dense Ring of Molecular Gas in NGC 1614

"Theories crumble, but good observations never fade."

HARLOW SHAPLEY (1885 - 1972)

asfa